THESIS

THE SPATIAL AND TEMPORAL PROPERTIES OF PRECIPITATION UNCERTAINTY STRUCTURES OVER TROPICAL OCEANS

Submitted by

Jianbo Liu

Department of Atmospheric Science

In partial fulfillment of the requirements

For the Degree of Master of Science

Colorado State University

Fort Collins, Colorado

Spring 2015

Master's Committee:

Advisor: Christian D. Kummerow

Christopher W. O'Dell
Steven C. Reising

ABSTRACT

THE SPATIAL AND TEMPORAL PROPERTIES OF
PRECIPITATION UNCERTAINTY STRUCTURES OVER TROPICAL OCEANS

The global distribution of precipitation has been measured from space using a series of passive microwave radiometers for over 40 years. However, our knowledge of precipitation uncertainty is still limited. While previous studies have shown that the uncertainty associated with the surface rain rate tends to vary with geographic location and season, most likely as a consequence of inappropriate and inaccurate microphysical assumptions in the forward model, the internal uncertainty structure remains largely unknown. Hence, a classification scheme is introduced, in which the overall precipitation uncertainty consists of random noise, constant biases, and region-dependent cyclic patterns. It is hypothesized that those cyclic patterns are the result of an imperfect forward model simulation of precipitation variation associated with regional atmospheric cycles. To investigate the hypothesis, differences from ten years of collocated surface rain rate measurements from TRMM Microwave Imager and Precipitation Radar are used as a proxy to characterize the precipitation uncertainty structure. The results show that the recurring uncertainty patterns over tropical ocean basins are clearly impacted by a hierarchy of regionally prominent atmospheric cycles with multiple time scales, from the diurnal cycle to multi-annual oscillation. Spectral analyses of the uncertainty time series have also confirmed the same argument. Moreover, the relative importance of major uncertainty sources varies drastically not only from one basin to another, but also with different choices of sampling resolutions. Following the classification scheme and hypothesis

proposed in this study, the magnitudes of un-explained precipitation uncertainty can be reduced up to 68% and 63% over the equatorial central Pacific and eastern Atlantic, respectively.

ACKNOWLEDGEMENTS

The work presented here would not have been possible without the help from various individuals. First and foremost, I would like to deeply thank my advisor, Dr. Chris Kummerow, for his guidance and support throughout this study. I also would like to extend my gratitude to my committee members, Dr. Chris O'Dell and Dr. Steven Reising, for their valuable comments on my work. I sincerely thank the entire Kummerow research group for their help and encouragement during my master program. I am also very grateful for my family and friends, especially my girlfriend Yanru Tang, for their emotional support throughout this journey. In addition, this study is partially funded by NOAA grant NA1HOARH4320125.

TABLE OF CONTENTS

CHAPTER 1

INTRODUCTION

Precipitation serves as one of the most important coordinators controlling global and regional hydrological balance and energy equilibrium. Water in its various forms travels unceasingly among the atmosphere, biosphere, land, and ocean, as it keeps the hydrological cycle in general balance (Fig. 1.1, Oki and Kanae 2006). The transport, however, is rarely smooth but instead sporadic, causing severe water deficiency (like droughts) over one region and excessive water supply (like floods) at another place. At the same time, imbalanced surface energy is removed mostly through evaporation and released to the atmosphere via the latent heat of condensation. While in its vapor form, latent heat from the water vapor can be transported over long distances through large-scale atmospheric motions. Once condensed, the drop will generally fall as precipitation. Hence, precipitation is not only serving as the heat transporter, but also as a sensitive indicator of Earth's energy balance.

A variety of measuring systems have been developed historically to retrieve rainfall information. More than 3500 years ago, astrologers in ancient China started to inscribe symbols on ox bones or turtle shells to record the eye-witnessed weather phenomena (mostly the extreme rainfall events) for fortune-telling purposes (Wang and Zhang 1988). Around 500 B.C, ancient Greeks and ancient Indians recorded the rainfall amount to deduce the expected crop yields, and used it as a basis for calculating the land tax (Strangeways 2010). During the Age of Discovery, Portuguese adventurers found prevailing wind systems over the Atlantic, and most likely the associated raining regions. In 1694, Richard Towneley, an English mathematician and astronomer, first discussed the rainfall differences over different parts of England using 15 years of systematic records of rainfall measurements (Towneley 1694). During World War II,

scientists from the Great Britain and the United States` started to use radar to explore rainfall properties associated with tropical cyclones.

Complete global rainfall measurements finally became feasible in the early 1960s, when precipitation could be observed from satellites. The first attempt to estimate precipitation over ocean using a spaceborne microwave radiometer was accomplished by the Electrically Scanning Microwave Radiometer (ESMR) aboard the Nimbus 5 satellite. ESMR was a single channel, horizontally polarized radiometer, operating at 19.35 GHz. Allison et al. (1974) used an empirical relationship between the measured brightness temperatures and collocated surface rain rates to estimate the rainfall intensity. Given that the observed brightness temperatures depend not only on the rain rate, but also the surface temperature, its emissivity, as well as cloud water and water vapor, the empirically derived results were likely to be biased (Munchak 2010). More robust estimates could not be made until precipitation information could be retrieved from multiple channels, such as from the Scanning Multichannel Microwave Radiometer (Gloersen and Hardis 1978). In the late 1980s, the Special Sensor Microwave Imagers (SSM/I) aboard the Defense Meteorological Satellites Program (DMSP) satellites used seven microwave channels to infer surface rain rates. Another decade later, the Tropical Rainfall Measuring Mission (TRMM) was launched to simultaneously measure collocated rainfall events from a passive microwave imager and active centimeter-wavelength radar.

At the beginning of the new millennium, a series of Advanced Microwave Scanning Radiometers (AMSR), and the successor AMSR-Earth Observing System, were sent to the space to gather information about water sources in the Earth's system (Kawanishi et al. 2003). In February 2014, the launch of the Global Precipitation Mission (GPM) core observatory extended the region of active and passive observations (as compared to TRMM) from the extra-tropics up to 68° latitudes in both hemispheres (Hou et al. 2014). Furthermore, the GPM Microwave Imager

(GMI) adds additional 4 high frequency channels to enhance its ability to detect precipitation in solid forms over high-latitude areas. Despite the continuously increasing observational capabilities and accompanying improvements in precipitation products, there has been little progress in quantifying uncertainties from the precipitation retrievals. This study seeks therefore to build a specific framework for computing uncertainties in one of the TRMM precipitation products – the passive microwave rainfall estimations, or 2A12 in its latest version (Version 7). The framework has been designed to be readily applicable to rainfall estimates produced by other passive microwave sensors as well.

1.1 Background

In the conventional way of defining measurement uncertainties, differences between the measurement and a specified "truth" are quantified as a combination of systematic and stochastic errors. Stochastic uncertainty from the satellite rainfall products can be quite large and critical for researchers who complete their work utilizing short-term and/or localized precipitation observations. Its relative importance, however, reduces quickly for climatological or large-scale research applications due to the signal cancellation of random noise. Systematic uncertainties, on the other hand, are rarely numerically uniform from a global rainfall perspective, instead varying with different meteorological regimes. Stephens and Kummerow (2007) argued that the bulk precipitation uncertainties look neither random (completely unpredictable) nor systematic (constant over space and time), but more like a mixture of both. Moreover, the majority of the bulk error seems to associate with the construction of the forward model, which tends to vary with cloud and precipitation regimes. Numerous studies have confirmed their statements. Examples detailing the spatial and/or temporal discrepancies among different precipitation products are presented below.

Masunaga et al. (2002) made one of the earliest attempts to discover the inconsistencies between TMI and PR rainfall products, in which they found that the biases had a strong regional dependence. In mid-latitudes, PR tended to over report the near-surface precipitation water content (PWC), especially in winter, which was most likely due to the limitation of the pre-existing TMI profiling database. In tropics, however, PR produced much less precipitation water path (PWP) because of its algorithmic deficiency. Moreover, for a given PWC or PWP, TMI algorithm yielded a larger rain rate than PR. The authors then argued that the biases arose from a combined result of the different physical measuring principles between the two sensors and a PR algorithm-based precipitation water path-to-rain rate conversion scheme.

Adeyewa and Nakamura (2003) compared the monthly averaged TRMM PR data to the surface rain gauge network over major climatic zones in continental Africa, and the biases showed apparent seasonal and regional variability. In general, the biases reached the annual maximum during local dry seasons, whose occurrence varies by latitudes. By further taking the zonal-mean precipitation analysis, they found PR severely overestimated (by more than 30%) the rainfall over the tropical-rain-forest region (between 6.5°S and 6.5°N) during the northern hemispheric wintertime. As a result, they concluded that the TRMM PR data was only reliable over northern and southern savanna regions (around 10°N and 20°S, respectively) during the wettest season of the year.

Rajendran and Nakazawa (2005) compared the conditional surface rain rates (the average rain rate of all raining pixels within a pre-defined domain) between TMI and PR, and found that TMI estimates were generally larger than PR estimates for most part of the equatorial oceans. Through analysis of the convective rainfall percentages associated with the precipitation, the differences were likely related to different life stages of organized convections in the tropics. To be more specific, PR showed excessive rain in situations of low TMI convective percentages and

high PR convective percentages, which represented the formative stage of convections. The opposite, TMI overestimating the rainfall, often occurred during the mature-to-decaying stage of convection, when high TMI convective percentages and low PR convective percentages were often witnessed. Finally, the authors listed several reasons that may contribute to this systematic bias, which includes the existence of overshooting cloud tops, the time lag between the maximum rain rate and the highest cloud top height, the increased backscattering signals due to cloud ice crystals, and the presence of melting layer.

Berg et al. (2006) examined a number of physical variables that can be used to explain the observed regional-dependent systematic precipitation detection differences between TMI and PR. The differences were mostly discovered along the mid-latitudes storm tracks, where only the higher-resolution PR can pick up rainfall signals from isolated convective trailing frontal systems. On the other hand, TMI captured light-to-medium rainfall over East China Sea, where radar signals are generally below the PR detection threshold. A following study by Berg et al. (2008) showed that high local aerosol concentrations could lead to an increase in the ratio of cloud water to rain water within the column, as well as postpone the initiation of warm rain processes.

Yamamoto et al. (2008) explored daily variability of measured precipitation from TMI, PR, and the Visible and Infrared Scanner, which was onboard the TRMM satellite as well. Temporally as well as regionally dependent systematic biases were detected as the local peak raining times were shifted by a few hours among the three sensors. The phenomena were most profound over the plateau sections and the Gulf of Mexico. Further investigations were conducted to explain the systematic peak time shifts, and they found that the time shift was sensitive to the amplitude of diurnal variation (i.e., land vs. ocean), convective rainfall frequency, and storm heights. Therefore, they claimed that the observed time shifts could be tied to the

evolution of convective systems, and the shifts were mainly caused by the different detection capabilities of each sensor.

Wang and Wolff (2012) performed the comparisons between the TMI rainfall estimates and the ground-based validation measurements (including radar and tipping-bucket rain gauges) over the TRMM Ground Validation site at Melbourne, Florida. The TMI measurements showed small negative biases during the 12-year studying period, with only a few exceptions. In terms of rain rates, TMI gave a much better performance over light rainfall compared to higher rain rates. Moreover, despite the fact that diurnal cycles of precipitation were well captured by both TMI and the ground site, there was about a one-hour time lag between the spaceborne sensor and the ground instruments, mostly due to the ice aloft which is consistent with the findings from Yamamoto et al. (2008) mentioned above.

Based upon the aforementioned studies, the precipitation uncertainties have shown clear fluctuating characteristics that cannot be captured by a simple combination of two fixed values, i.e., the random and systematic uncertainties. Instead, an uncertainty-quantifying model should, at a minimum, contain enough structures to capture the uncertainty variations mentioned above.

Unlike some recent work (Adler et al. 2012; Maggioni et al. 2014) that had primarily focused on the systematic or stochastic uncertainty individually, trying to capture the general external features of the measurement uncertainty, this work features an in-depth look into the chaos inside the uncertainty, trying to disentangle the overall uncertainty into a hierarchy of relatively well-known constituents. Although some of those constituents appear to be independent from each other, they are more-or-less physically and mathematically connected via the observing mechanism and retrieval algorithm. While this study will only provide qualitative uncertainty numbers, the analyses utilize the difference between TRMM radar and radiometer rainfall products to provide a guide for building a comprehensive uncertainty model. Meanwhile, by

describing the characteristics of the uncertainty field, especially where large discrepancy occurs, it may shed light on regional rainfall retrieving defects that need to be fixed in the retrieval algorithm.

1.2 Precipitation Uncertainty Analyses

The sources of precipitation uncertainty can be quite complicated. This section will illustrate major uncertainty sources from the current TMI rainfall retrieval algorithm via multiple examples.

The majority of TMI retrieval uncertainties act as a combination of stochastic and systematic components, which vary with space and/or time. In terms of individual uncertainty source, both components typically exist simultaneously, but often not of equal importance. For convenience, major uncertainty sources will be categorized as either random or systematic based on their predominant characteristics; in other words, a random uncertainty source may still retain its systematic portion, but behave more randomly under most frequent circumstances. Since a large portion of the overall uncertainty comes from the forward model, uncertainties associated with the forward model, including both random and systematic sources, are discussed independently at the end of this section.

1.2.1 Random Uncertainty Sources

Technically, random uncertainties are the unpredictable unknowns in measurements that can lead to measured values being inconsistent among multiple repeated measures (Taylor 1999). Random uncertainties have arithmetic means equal to zero, and their probability functions are considered to follow Gaussian distributions. Three common sources of random uncertainty in the

current TMI retrieval are considered to be the instrument noise, sampling limitation, and algorithmic ambiguity.

Channel-dependent instrument noise is relatively small with the current state-of-the-art microwave radiometer, typically on the order of a few tenths of a Kelvin. Every radiometer has a noise value, or the "noise-equivalent temperature variation", which is sensitive to both frequency and polarization. Despite the fact that the channel noise itself is normally distributed, the extent to which it will shape the distribution of the retrieved quantity, such as precipitation, is still unknown and left to be determined. Details of instrument noise associated with each TMI channel are given in Table 1.1.

Another typical random measurement uncertainty source stems from the sampling limitation. Non-geostationary satellites can only fly over the same region once or twice per day. Hence, rainfall accumulation in particular, will have errors based upon this limited sampling strategy. For long-term climatological precipitation property, such as the annual mean rain rate, the sporadic observations are considered to be statistically stable. For short-term rainfall accumulation, such as the daily rainfall accumulation, however, the sampling uncertainty becomes more problematic (Maggioni et al. 2014), as an instantaneous rainfall observation of 5mm/hr at noontime does not imply the atmosphere will keep raining at the same intensity for the entire day. Given TRMM's non-sun synchronous sampling strategy and an emphasis on climatological rainfall uncertainty in this study, the author will treat sampling uncertainty as random in this work.

Finally, due to the incomplete knowledge about the environmental condition, inverse problems are generally ill posed and may contain multiple solutions (Rogers 2000). As a result, a close match between the modeled and measured brightness temperatures (Tb) sometimes cannot guarantee a unique retrieval of the vertical hydrometeor profile. The ambiguity issue is

particularly noteworthy when two vertical rainfall profiles with difference surface rain rates have indistinguishable Tb at TMI frequencies, as illustrated in Kummerow et al. (2011). However, the impact is secondary as compared to the previous two, and can be reduced, if additional pieces of information, such as an extra radiometer channel or a collocated radar reflection, are supplied to make the similar rainfall structures distinguishable.

1.2.2 Systematic Uncertainties Sources

Imperfect sensor calibration contributes to a small fraction of the systematic uncertainty. For example, the TMI warm point calibration is established at every revolution with respect to a warm reference load. This reference is theoretically expected to emit like a blackbody at a fixed temperature (usually around 280 K). In reality, there will always be discrepancies between the "assumed" temperature and the "true" temperature measured by the sensor, which leads to systematic biases in the measured brightness temperatures. The sensor calibration bias is often uniform over time and space, and causes uncertainties in the precipitation retrieval.

Another type of commonly seen systematic uncertainties comes from the instrument limitations, as each sensor has its preferential precipitation detecting regimes. For example, PR is incapable of detecting rain rate below 0.5 mm/hr because small rain droplets are nearly invisible to the centimeter-wavelength radar pulses. At the same time, higher frequency TMI channels saturate quickly in the heavy precipitation scenarios, which impairs the instrument sensitivity. Consequently, instrumental limitation is intrinsic to the sensor, and may vary systematically among individual rainfall regime.

1.2.3 Uncertainties Associated with the Forward Model

Stephens and Kummerow (2007) pointed out that the leading source of retrieval uncertainties should arise from the cloud microphysical assumptions that are made during the construction of the forward model. The forward model can be schematically broken down into two basic modules – an atmospheric model parameterizing the cloud and precipitation structures imbedded in the rainfall event, and a radiative transfer model simulating the brightness temperatures at top of the atmosphere that are observed by the radiometer. For both modules, empirical and sometimes even unrealistic assumptions about certain microphysical parameters have to be made in order to complete the model, such as fixed ice density and spherical treatment for ice particles. More often than not, those parameters are integral parts of the forward model, which makes them hard to be dissembled and therefore inspected individually, without mentioning the frequent absence of well-characterized validation sources. To make the complexity even worse, for those ancillary parameters that are physically retrieved as inputs to the model, such as the liquid water path, their uncertainties are typically not quantified and would probably vary if the retrieving method changes. As a result, it is neither feasible nor meaningful to separate the forward model uncertainty into individual sub-components, which is also why the forward model uncertainty is so elusive to comprehend. The majority of forward model uncertainty looks neither random nor systematic, but more like a mixture of both. To simplify the discussion, more random-behaved model uncertainties will be introduced first, followed by the description of the more systematically behaved uncertainty components.

An example of the random model uncertainty is the parameterization of cloud ice density in the cloud-resolving model. Although the density of ice particles within a mixed phased cloud system is likely to vary from one part of the cloud to another, the cloud ice density is a fixed mean value computed from limited number of studies. Hence, the model results are sensitive to

the pre-assigned density value, so that the any small density perturbation would lead to multiple distinctive but plausible retrievals for the column ice content as well as vertical distribution. Moreover, physical retrieval of ice density is not readily achievable and may require additional assumptions, which would further complicate the issue. As a result, the inevitable artificial assumptions of cloud ice density, together with many other cloud microphysical parameters, remains an untreatable (and may be even unsolvable) portion of the precipitation uncertainty in this study.

The more systematic-like portion of the forward model uncertainty, on the other hand, is assumed to be one of the most important components in the overall precipitation uncertainty. Together with its random counterpart, their impact could be as much as an order of magnitude larger than any other individual uncertainty source. Fortunately, most random components reduce quickly in terms of their magnitudes with averaging because of their Gaussian-distributed nature, and eventually give statistically nearly unbiased climatological answers. The systematic-behaved forward model uncertainties, which are often the result of parameterizing the precipitating conditions using long-term mean (or empirical) values. Despite the qualitative resemblance that may be achieved by utilizing the long-term mean values, the actual region-to-region precipitation parameters, such as drop size distribution, hardly replicates the mean state close enough. Hence, if these forward model assumptions are not allowed to change with rainfall regimes, they will cause regime-dependent biases as illustrated in Berg et al. (2006). Two examples regarding the systematic forward model uncertainty are discussed below.

Munchak et al. (2012) retrieved the drop size distribution (DSD) from two years of TRMM radar-radiometer combined algorithm, and characterized the DSD in relation to the vertical hydrometeor profile, mesoscale organization, and background environment. Small reflectivity-normalized median drop sizes were often observed in the tropics, especially in the large shallow

convective system where the warm rain processes dominated. Alternatively, large median drop size values were found in scattered convection associated with the passage of extratropical cold front. The authors concluded that the precipitation difference between the TMI and PR associated with the DSD variations were mostly likely due to either the insufficient DSD adjustment in the PR retrieving algorithm or the incorrect description of the DSD as well as vertical profiles in the TMI hydrometeor database.

Petkovic and Kummerow (personal communication) showed strong region-dependent biases in the surface precipitation when comparing the TMI surface rain rates to PR over the Amazon and central-west Africa, respectively. The authors found that the retrieved rainfall amounts were quite sensitive to the amount of ice particles present in the precipitating clouds, which was affected by local environmental conditions, such as the convective available potential energy (CAPE), wind shear, and vertical humidity profile. By appropriately accounting for the three variables, they could reduce local rainfall bias by as much as 30%.

In summary, uncertainties resulting from the imperfect forward model simulations contribute to a substantial portion of the total measurement uncertainty. Although multiple uncertainty sources introduced by the forward model have been speculated, some of which had already been verified, the overall forward model impact on the final precipitation product still remains largely unknown.

1.3 Overview of Thesis

It is clear from the preceding discussion that satellite-retrieved precipitation uncertainties are nowhere close to a constant number. Instead, previous peer studies have shown that the uncertainty tends to vary systematically from one region to another and similar uncertainty features are inclined to reveal themselves in a periodic manner, such as the strong positive biases

over the East China Sea observed only during the northern hemisphere wintertime (Berg et al. 2006). Despite numerous factors that could have contributed to the total uncertainty, Stephens and Kummerow (2007) argued that the majority of precipitation uncertainty results from the inadequate and inappropriate microphysical assumptions in the forward model. In reality, microphysical parameters are physically connected with the ongoing atmospheric dynamics, which are inclined to repeat themselves over unique rainfall regimes. It is therefore reasonable to speculate that the retrieved precipitation uncertainty would behave in a similar manner.

The author is therefore proposing that: 1) the total precipitation uncertainty can be described by two independent but internally connected components – stochastic and systematic uncertainties, and that systematic component would further contain region-dependent constant biases as well as certain recurring patterns; 2) those recurring patterns mainly result from the forward model simulation of the locally prominent atmospheric cycles, and consequently contain temporal and spatial variability.

A detailed description of primary sensors and observational data utilized in this research will be introduced in Chapter 2. In Chapter 3, the author will first show the property and impact of stochastic uncertainty at the instantaneous scale as well as its temporal propagating characteristics. Then, systematic precipitation uncertainties will be analyzed over several carefully chosen tropical oceans, with each of those regions containing one dominant atmospheric cycle selected from a broad range of time scales (from diurnal cycle to multi-annual oscillation). Beginning with a qualitative estimation of major uncertainty partitions over the central-to-eastern tropical Pacific, Chapter 4 will then explore how different regional atmospheric cycles influence the uncertainty structures simultaneously and how different uncertainty sources contribute to the overall precipitation uncertainty. This is followed by a similar experiment but performed over a different tropical ocean basin to highlight regional

discrepancies in the uncertainty structures. Eventually, the uncertainty classification framework, which evaluates different uncertainty sources on an individual basis, will be revisited in its entirety at the beginning of Chapter 5, followed by concluding remarks and suggestions for future work.

CHAPTER 2

DATA

In this chapter, the author will first present a quick review on the satellite configuration and instrument specifications of two major onboard sensors that are used to depict precipitation uncertainty structures in this work. Then, the precipitation retrieval scheme for the passive radiometer and active radar will be discussed in detail, as this work attempts to build a framework to characterize the rainfall uncertainty, based upon the difference of two nearly independent rainfall measurements - the TMI and PR. TMI uses microwave brightness temperatures, radiative transfer schemes, and a Bayesian-based retrieval algorithm to find the mostly likely surface rain rate. On the other hand, PR surface rainfall quantification relies heavily on the signal reflected by the hydrometeors, as well as the signal attenuation over the rainfall column. Since the detecting principles of two sensors are fundamentally independent from each other, the difference between those two products (i.e., TMI minus PR) should characterize the precipitation uncertainty with the broadest range possible.

2.1 Tropical Rainfall Measuring Mission (TRMM) and Major Instruments Specifications

Carrying instruments to measure precipitation and energy budget within the tropical atmosphere, the TRMM satellite was launched into a non-sun synchronous orbit in late 1997, and has been providing consistent and reliable monitoring data for more than 17 years (Kummerow et al. 1998). The satellite orbits earth approximately 16 times per day, scanning up to 35° in latitudes for both hemispheres. Its initial altitude was 350km, but was boosted to a higher altitude of 402.5km in August 2001 to reduce fuel consumption. All precipitation data used to calculate the uncertainty in this work are selected from the post-boost period to prevent any unnecessary

biases due to the orbital change (DeMoss and Bowman 2007). Moreover, on May 29, 2009, the original (A-side) electronic interface stopped working and it took the mission team approximately 2 weeks to investigate the reason and switch to the redundant electronics, as reported by Japan Aerospace Exploration Agency. Although this malfunction resulted in slight but noticeable change in the PR precipitation retrievals, the author decides to ignore the impact and replace 20-day of missing PR observations (from May 29 to June 19) with climatological mean values.

2.1.1 TRMM Microwave Imager

The TRMM Microwave Imager (TMI) is a nine-channel passive microwave radiometer that measures brightness temperatures (TB) at five frequencies: 10.7, 19.4, 21.3, 37.0, and 85.5 GHz (Kummerow et al. 1998). Dual-polarimetric measurements are available at 10.7, 19.4, 37.0, and 85.5 GHz channels. Compared to its technical predecessors (i.e., SSM/I), the TMI added a pair of low frequency channels at 10.7 GHz and moved the water vapor channel from 22.235 GHz to 21.3 GHz to avoid water vapor saturation in the tropics.

The TMI antenna rotates at a constant speed of 31.6 revolutions per minute and receives microwave signals at an incident angle of 52.8 degrees with respect to the Earth's surface (Fig.2.1, Kummerow et al. 1998). The conical scanning geometry allows 130 degrees from the forward direction to be used to collect data, while leaving the rest 230 degrees for calibration and housekeeping purposes. The forward 130-degree arc yields a swath of 759km in the cross-track direction with a spacing of 13.9 km between pixels from two successive scans. A more detailed instrument description is available in Kummerow et al. (1998).

2.1.2 Precipitation Radar

The first space-borne Precipitation Radar (PR), operates at 13.8 GHz (Ku-band) and scans ±17° from nadir with 49 cross-track pixels. This results in a swath of 247 km (post-boost) that covers the central one-third of the TMI swath. The radar has a footprint size of 4.3km (which is similar to the footprint size of an 85 GHz TMI pixel) at nadir and a vertical resolution of 250m. The radar was designed to have a minimum detectable threshold of 17 dBz, which corresponds to approximately 0.5 mm/hr in rain rate. The TRMM PR can measure 3-D structures of rainfall events and provide additional hydrometeor information, such as precipitation type (convective vs. stratiform). More instrument details can also be found in Kummerow et al. (1998).

2.2 Rainfall Retrieval Algorithms

2.2.1 Rainfall Retrieval Algorithm for TMI

The Goddard Profiling Algorithm (GPROF) is a microwave-based rainfall retrieval algorithm, which was originally developed for the SSM/I sensors on the DMSP satellites (Kummerow et al. 1996). For implementing in TRMM operations, the algorithm has undergone several major modifications (Kummerow et al. 1996; Kummerow et al. 2001; Kummerow et al. 2011). It has become the operational rainfall retrieval algorithm for TMI, AMSR-E, AMSR2, and SSM/I instruments since then. The GPROF is able to obtain 3-D rainfall structures and the associated hydrometeor environment. In this study, only surface rain rates will be used. Data can be obtained from the official NASA TRMM website (http://trmm.gsfc.nasa.gov/).

The retrieval algorithm can be divided into two parts: the rainfall retrieval over the ocean which is primarily based on the Bayesian probability theorem, and the land retrieval which is based on empirical relationships between the ice-scattering signals at high-frequency channels and the instantaneous surface rain rates. For completeness, both retrievals will be briefly

discussed in this section. Detailed retrieving procedures can be found from Kummerow et al. (2001, 2011).

2.2.1.1 TMI Retrieval over the Ocean

Over the ocean, the Bayesian-based rainfall retrieval can be symbolically expressed as (Kummerow et al. 2001):

$$\Pr(\mathbf{R}|\mathbf{TB}) = \Pr(\mathbf{R}) \times \Pr(\mathbf{TB}|\mathbf{R}) \tag{2.1}$$

Where **R** is the vertical hydrometeor profile, **TB** is the brightness temperature vector from all frequencies, $\Pr(\mathbf{R}|\mathbf{TB})$ is the posterior probability of observing **R** given the observed brightness temperature vector **TB**, $\Pr(\mathbf{R})$ is the prior probability of observing the given hydrometeor profile of **R**, and $\Pr(\mathbf{TB}|\mathbf{R})$ is the probability of observing brightness vector **TB** for the hydrometeor content **R**.

The prior probability of profile **R** (i.e., $\Pr(\mathbf{R})$) is calculated from the relative number of occurrences observed by the TRMM precipitation radar. A radiative transfer scheme is used to derive the brightness temperature vector **TB** at the top of the atmosphere, as it would be seen by the TMI. As a result, using the Bayes' theorem, the term on the left-hand side is readily calculable. Finally, if assuming the observed and simulated error distributions are Gaussian, the optimally retrieved rain rates $\widehat{\mathbf{R}}$ are given by the minimum variance solution:

$$\mathrm{E}\left(\widehat{\mathbf{R}}\right) = \sum_{\mathrm{i}} \mathbf{R}_{\mathrm{i}} \frac{\Pr(\mathbf{R}_{\mathrm{i}}|\mathbf{TB})}{\mathbf{A}} \tag{2.2}$$

and the conditional probability $\Pr(\mathbf{R}_{\mathrm{i}}|\mathbf{TB})$ and normalization factor **A** can be expressed as:

$$\Pr(\mathbf{R}_{\mathrm{i}}|\mathbf{TB}) = \exp\left\{-\frac{1}{2}[\mathbf{TB}_{\mathrm{obs}} - \mathbf{TB}_{\mathrm{model}}(\mathbf{R}_{\mathrm{i}})]^{\mathrm{T}}(\mathbf{O}+\mathbf{M})^{-1}[\mathbf{TB}_{\mathrm{obs}} - \mathbf{TB}_{\mathrm{model}}(\mathbf{R}_{\mathrm{i}})]\right\} \tag{2.3}$$

$$\mathbf{A} = \sum_{\mathrm{i}} \exp\left\{-\frac{1}{2}[\mathbf{TB}_{\mathrm{obs}} - \mathbf{TB}_{\mathrm{model}}(\mathbf{R}_{\mathrm{i}})]^{\mathrm{T}}(\mathbf{O}+\mathbf{M})^{-1}[\mathbf{TB}_{\mathrm{obs}} - \mathbf{TB}_{\mathrm{model}}(\mathbf{R}_{\mathrm{i}})]\right\} \tag{2.4}$$

where $\mathbf{TB}_{\mathrm{obs}}$ is the observed TB vector, $\mathbf{TB}_{\mathrm{model}}(\mathbf{R}_{\mathrm{i}})$ is the simulated TB vector for the given hydrometeor profile $\mathbf{R}_{\mathrm{i}}$, $\mathbf{O}$ and $\mathbf{M}$ are the observation and model error covariance matrices, respectively.

To minimize the computational cost during daily routine operations, all the probabilities on the right-hand side of Eqn. (2.1) are calculated in advance and stored in a database, also known as the a-priori database. Further details about the a-priori database are detailed in Kummerow et al. (2011).

2.2.1.2 TMI Retrieval over Land

The rainfall retrieval over land contains less physics, when compared to its ocean counterpart. Unlike the cold ocean surface in the microwave band, the emissivity of the land is much closer to 1, which makes it quite difficult for the TMI to distinguish raining hydrometeors from the surface background. The wide variation of topography, vegetation types, and soil moisture further complicates the problem. As an alternative to the emission-based approach, the TB depressions at 85 GHz (due to scattering by ice or large rain drops) are statistically related to the instantaneous surface rain rates (Spencer 1986; Grody 1991). Moreover, a screening procedure is performed to differentiate the raining scenes from radiometrically cold surfaces (e.g., snow, desert) that may otherwise be confused with precipitation (Ferraro et al. 1998). In addition, since convective and stratiform rainfall behave differently from each other in terms of their empirical TB relationships, the surface rainfall is given by the sum of the weighted contributions from both the convective and stratiform rainfall (McCollum and Ferraro 2003), which can be expressed as:

$$\mathrm{Rain}_{\mathrm{land}} = \Pr(\mathrm{convective}) \times \mathrm{Rain}_{\mathrm{convective}} + \Pr(\mathrm{stratiform}) \times \mathrm{Rain}_{\mathrm{stratiform}}$$

where: $\mathrm{Rain}_{\mathrm{land}}$ is the overall rain rate retrieved by the GPROF, $\Pr(\mathrm{convective})$ is the probability of convective rainfall, $\mathrm{Rain}_{\mathrm{convective}}$ is the convective rain rate derived from the

empirical TB relationship, $\mathrm{Pr}(\mathrm{stratiform})$ is the probability of stratiform rainfall, $\mathrm{Rain}_{\mathrm{stratiform}}$ is the stratiform rain rate derived from the empirical TB relationship.

Wang et al. (2009) point out that the retrieval algorithm may fail to detect warm rain processes due to the lack of ice-scattering signals from the liquid cloud, while it is more likely to overestimate rain rates in strong convective clouds that tend to produce a lot more ice crystals. Liu and Zipser (2005) concluded that regionally dependent errors would occur if the ratio of the 85 GHz ice scattering signal to rain rate was assigned improperly. Since this study focuses strictly on ocean retrievals, there will not be any further discussions regarding the possible systematic biases of the TMI rainfall retrieval over land.

2.2.2 Rainfall Retrieval Algorithm for PR

Similar to most ground-based radars, the TRMM PR uses a power law relationship between radar reflectivity Z and rainfall rate R to convert radar echo intensities into rainfall rates:

$$Z = aR^b$$

where coefficient a and exponent b are empirical constants for given drop size distributions. As these constants are typically not known, the PR uses a hybrid of the surface reference method (SRT, Meneghini et al. 2000) and the Hitschfeld-Bordan method (Iguchi and Meneghini 1994) to determine the signal attenuation (Iguchi et al. 2000).

At 13.8 GHz, raw radar echoes suffer from appreciable amount of attenuation due to atmospheric gases, aerosols, and hydrometers. The PR rainfall retrieval algorithm treats the attenuation in two ways: the attenuation due to cloud liquid water, water vapor and molecular oxygen is empirically calculated from the radar-measured variables; the attenuation caused by precipitation is estimated using the hybrid method mentioned above. In this method, path-integrated attenuation (PIA) is independently calculated using the Hitschfeld and Bordan (1954)

method and the SRT (computed by taking the difference of the normalized surface cross sections between a raining pixel and a nearby non-raining pixel). Then, a Bayesian-based method is used to retrieve the optimal PIA that can be best explained by the two independently calculated PIAs. Finally, an attenuation correction factor can be estimated from the optimal PIA, and applied to the measured reflectivity to retrieve the attenuation-corrected reflectivity.

After taking into account the non-uniform beam filling effect, the attenuation-corrected reflectivity is used to derive the vertical rain rate at each range gate where appropriate sets of a and b need to be chosen depending on a number of factors, such as the rain type, presence of bright-band, freezing height, and most importantly, their consistencies with respect to the optimal PIA. Detailed retrieving procedures can be found from Iguchi et al. (2000).

2.3 Collocated TMI and PR Surface Rain Rates

Hourly gridded TMI (Kummerow et al. 2001; Kummerow et al. 2011) and PR (Iguchi et al. 2000) surface rain rates (TRMM 3G68) are used in this study, at 0.5°×0.5° spatial resolution. The dataset can be obtained from NASA's Goddard Space Flight Center, via ftp at: ftp://trmmopen.gsfc.nasa.gov/pub. Additional information about the dataset is available from the Goddard DAAC TRMM information page. Ten years of surface rain rate measurement from the post-boost period, starting in January 2002 and ending in December 2011, are used to compute the precipitation uncertainty in this work, which is defined as the instantaneous surface rain rate difference between TMI and PR.

For each valid grid box (which requires at least one TMI pixel and one PR pixel in the same 0.5°×0.5° box), four rainfall parameters are stored independently: total rain volume reported by TMI, total number of pixels reported by TMI, total rain volume reported by PR, and the total number or pixels reported by PR. The mean grid box rain rate for each sensor is defined as the

total rain volume divided by the total number of pixels. For convenience, the dataset is further integrated into 1°×1° resolution, following the same recording standards. Results in Chapter 4 will show that sampling resolution will only impact the magnitude of the precipitation uncertainty without changing its first-order characteristics.

A snapshot of the collocated surface rain rate for January 1st, 2010, is shown in Figure 2.2. The upper panel (Fig. 2.2(a)) shows several TMI overpasses on that day, which covers nearly three times more area than PR does (Fig. 2.2(b)) because of TMI's wider sensor swath. The difference between the collocated TMI and PR is calculated, as shown in the bottom panel (Fig. 2.2(c)), with warm colors indicating TMI overestimations and cold colors indicating the opposite.

The precipitation uncertainty in this study is characterized by the difference in TMI and PR products. Because the two products are independent, this provides at least a method for estimating the qualitative behavior, if not the magnitude of the uncertainties. Furthermore, given that the true rain rates will never be measured (since no sort of measuring technique is free from errors), it is not practical for the precipitation uncertainty to be defined as the difference between the truth and actual measurement, and therefore alternatives must be sought to portrait the uncertainty structure. For example, the Intergovernmental Panel on Climate Change (IPCC) uses the model differences to represent the precipitation uncertainty, while the GPCP estimates its climatological uncertainty based on the measured monthly spread among multiple single-source and merged precipitation datasets (Adler et al. 2012). In this work, the difference between the collocated TMI and PR is used as the uncertainty proxy, and called the "precipitation uncertainty" hereafter, to represent the instantaneous measurement uncertainty, which includes both random and systematic components from both TMI and PR.

CHAPTER 3

RESULTS

In this chapter, the surface rain rate difference between the latest TMI (Version 7) and PR (Version 7) retrievals will be analyzed over multiple tropical ocean basins, as they approximately represent the radiometer-retrieved precipitation uncertainty structures. The total rain rate difference will be broken into stochastic and systematic components and their multi-dimensional propagation characteristics will be examined. It is valuable, as will be shown later in this chapter, to further break the systematic uncertainty into regional-dependent constant biases and specific periodic patterns that contain substantial spatial and temporal variability.

In this chapter, analyses of the random uncertainty and constant biases will be introduced first, for the sake of completeness. The main focus of interest is on the regional-dependent cyclic behaviors of the systematic uncertainty. According to the hypothesis proposed at the end of Chapter 1, the cyclic uncertainties are largely the result of the imperfect forward model simulation of local atmospheric cycles. To validate the hypothesis, the observed precipitation uncertainties will be tested over several carefully chosen tropical ocean basins to encompass as many atmospheric cycles as possible, and the results will show that the recurrent uncertainty patterns are likely to be associated with regionally predominant atmospheric cycles.

3.1 Random Uncertainty

3.1.1 Random Uncertainty at Instantaneous Scale

At the instantaneous scale, random uncertainty can sometimes play a dominant role within the overall retrieved precipitation uncertainty, especially in heavy precipitation scenarios. An analysis of a typhoon pixel, raining at 33.7 mm/hr, is shown in Figure 3.1. The TMI precipitation

retrieval algorithm (GPROF) has selected a group of 4650 hydrometeor profiles from the database, and assigned corresponding Bayesian weights to each of them. Twenty-two profiles (shown as the 22 asterisks in the figure) are found to exercise more impact on the final rain rate compared to the rest of the group. Furthermore, three profiles (with corresponding rain rates of 21, 38, and 55 mm/hr) are seen as having the greatest weights in the final solution. The magnitude of the rainfall uncertainty for this pixel, which can be approximated by visually checking the differences among those 3 profiles, is close to 18 mm/hr. The systematic uncertainty, determined from overall global mean rain rate difference over the 10-year period, is nonetheless close to 0.3mm/day. As a result, the random uncertainty for this heavy raining pixel is at least two orders of magnitude larger than its systematic counterpart.

3.1.2 Random Uncertainty Propagation

Despite the large impact from the random noise at the instantaneous scale, the magnitudes can decrease quickly as the dataset is integrated over longer time periods. For purely random noise, the uncertainty is characterized by the variance divided by the square root of the number of the averaged samples, according to classic statistics. A 10°×10° grid box is picked from the western Pacific (Fig. 3.2(a)) to illustrate the propagation of random precipitation uncertainty averaged over multiple integrating time periods, for the entire data period of 10 years.

Panels with black asterisks (Fig. 3.2(b)-(e)) show the observed TMI vs. PR rain rates averaged over 1 day, 5 days, 1 month, and 3 months, respectively. The slopes of the asterisks can be roughly understood as the PR-to-TMI mean rain rates ratio, and it is almost identical to the one-to-one relationship line (ORL) because TMI reports nearly the same rainfall amount as PR when averaged over the entire data period. The level of scatter of the asterisks, with respect to the ORL, represents the magnitude of the precipitation uncertainty. Integrating over longer periods,

the asterisks start to converge toward the ORL, indicating more and more random uncertainty is canceling out.

If assuming that all the precipitation uncertainties are randomly distributed (Fig. 3.2(f)-(i)), statistical laws can be applied to simulate the propagating behavior of random uncertainties. It is clear that the blue asterisks are converging faster toward the ORL than the black ones. More specifically, by averaging the rain rates over 3 months, the magnitude of the pure random uncertainty is reduced to a trivial level (shown as the nearly straight line with little scatter in Fig. 3.2(i)), while certain precipitation uncertainty remains in the observation and is shown as the moderate degree of scattering of the black asterisks in Figure 3.2(e). The contrast between two uncertainty groups indicates that the actual observed uncertainty (the black asterisks) is not purely random, and must have contained some non-random ingredients that would not average to zero.

3.2 Systematic Uncertainty

3.2.1 Geographic Distribution of Constant Biases

If all measurement uncertainties are randomly distributed, following the trend from Figure 3.2(f)-(i), the overall magnitude should be negligible after averaging data longer than one year. However, by averaging the global (TMI-PR) differences over the entire data period of ten years, clear geographical patterns are revealed in the results (Fig. 3.3), suggesting a possible intrinsic relationship between the rainfall uncertainty and regional climatological conditions. This geographic uncertainty distribution is similar to the results from Berg et al. (2006), who related the differences to the total precipitable water. Strong TMI overestimation is observed in the Central Pacific where the El Nino Southern Oscillation phenomenon prevails, as well as the "bulls-eye" feature over the East China Sea that is likely to be caused by locally high aerosol

concentrations (Berg et al. 2008). Meanwhile, negative uncertainties appear as the two flanks that originate from the west Pacific warm pool and extend toward the centers of the Pacific Ocean in both hemispheres, as well as the northern Indian Ocean in the tropics. Similar negative differences are also seen in the extra-tropical North Atlantic, the Gulf of Mexico, the Caribbean Sea, and the equatorial central Atlantic near the African side.

3.2.2 Periodic Uncertainty Patterns Associated with Local Atmospheric Cycles

Up to this point, two out of three major uncertainty groups have been introduced (i.e., random uncertainty and constant bias), while the cyclic patterns are left to be determined. Results of the relative contribution from the three factors (data have been integrated over 1-month, with spatial resolution of 1°×1°) are shown over four tropical ocean basins (Fig. 3.4) - northern Indian Ocean (54°E~75°E, 9°N~3°S), western Pacific warm pool (150°E~180°E, 12°N~0°N), central-to-eastern Pacific Ocean (144°W~124°W, 12°N~3°N), and equatorial eastern Atlantic (27°W~12°W, 9°N~3°S). Random uncertainties, in all four regions, only occupy the minimum fractions in spite of certain variations. Meanwhile, the magnitudes of constant biases vary quite dramatically from 15% to 50%, indicating strong region-dependent characteristics. The vast majority of total uncertainty with in each ocean basin (except for the central Pacific) cannot be appropriately explained. Given the previous argument on forward model uncertainty being the largest among all uncertainty sources, the un-explained uncertainty should result from the incorrect and inappropriate microphysical assumptions in the forward model. Moreover, those microphysical parameters are known to interact with local atmospheric regimes, which therefore result in cyclic characteristics in these uncertainties.

For the rest of this chapter, major characteristics of uncertainty (mostly the un-explained uncertainty) will be examined over several tropical oceans, in the hope of finding spatial and

temporal uncertainty variations that are associated with locally dominated atmospheric cycles, from diurnal cycle to multi-annual oscillation. There are two caveats before proceeding to the cyclic analyses: 1) influences from the random uncertainty will be ignored since most analyses are based on monthly climatology; 2) regional constant biases (as shown in Figure 3.3) will be removed prior to the analyses as needed.

Multiple grid boxes, which generally cover 10 to 20 degrees of area in both longitude and latitude, will be selected to analyze the local precipitation uncertainty within the defined area. For simplicity, boxes are selected such that the homogeneity within the box is as high as possible. Figure 3.5 illustrates the selection of an undesired grid box across the equatorial Atlantic. A dipole feature in the precipitation uncertainty field is evident in Figure 3.5(a), with positive uncertainties to the west half of the ocean and negative uncertainties to the east. The corresponding monthly climatological results, for TMI, PR, and the uncertainty, are showing quite smooth fluctuations throughout the year (Fig. 3.5(c)), where the climatological mean for any given month is defined as the mean value of the same months from the entire 10-year data period (i.e., 10 years of Januarys, 10 years of Februarys, so on and so forth). The main reason for this lack of signal comes from the positive/negative signal cancelation within the box-covered area. The same approach is then applied only to the negative uncertainty center near the African coast (Fig. 3.5(b)). This time, much larger seasonal variability (Fig. 3.5(d)) are observed by both sensors (up to 4mm/day for TMI and 3mm/day for PR) and the uncertainty (up to 2mm/day), which also serves as strong evidence for the presence of seasonal precipitation uncertainty variation over this region.

3.2.2.1 Diurnal Cycle

The diurnal cycle of the surface skin temperature over the ocean is less prominent than over land, as the water can hold much more heat per unit mass. The smoother diurnal fluctuation in the sea surface temperature generally leads to a flatter rainfall distribution throughout the day. In addition, the precipitation over the ocean tends to peak in the early morning (Nesbitt and Zipser 2003), while the land precipitation peak usually occurs in the mid afternoon when the boundary layer stability is compromised due to solar heating. A grid box of 10°×10° in the eastern equatorial Indian Ocean captures the diurnal variability of precipitation uncertainty during the Asian-Australian summer monsoon seasons (June, July, and August, see Fig. 3.6(a)).

Two maximum rainfall peaks are observed by TMI around 06 and 18 in local time, respectively (blue line, Fig. 3.6(b)). The first peak is likely to be the morning ocean-driven stratiform precipitation, while the second peak could be associated with the convective precipitation due to unstable boundary layer conditions in the mid-to-late afternoon. In comparison, PR only captures the afternoon rainfall peak that is thought to be convection dominated (red line, Fig. 3.6(b)). This results in a sinusoidal precipitation uncertainty with positive values before the local noontime and negative values in the afternoon, as in Figure 3.6(c). However, it is not uncommon to witness TMI overestimating stratiform rainfall while underreporting convective rainfall, which are mostly caused by distinctive environmental conditions exhibited by the two types of rainfall (Nesbitt et al. 2004).

Further investigations have revealed that the diurnal cycle in the uncertainty field can only be observed during the summer monsoon seasons. For the non-monsoon seasons when the afternoon convection is less vigorous, the magnitude of diurnal uncertainty cycle after the local noontime is much less vigorous (not shown here). As a consequence, for an imaginary “complete” error-predicting model that is trying to capture the diurnal uncertainty cycles, it is of vital

importance to include a general circulation module to be able to resolve synoptic-scale meteorological systems, which includes but is definitely not limited to the summer monsoon system mentioned above.

3.2.2.2 Multi-Month Cycle

The central-to-eastern Indian Ocean provides an ideal bed for spawning the Madden-Julian Oscillation (MJO), which propagates to eastward with a speed close to 5 m/s (Elleman 1997). A collection of 23 MJO events (Table 3.2), most of which are chosen from the northern hemispheric cooler months to avoid confusion or interaction with the Asian-Australian Monsoon seasons, has been analyzed to explore how the precipitation uncertainty behaves during MJO events.

Author uses a "moving coordinate" technique (Elsaesser and Kummerow 2012) to follow the MJO-impacted precipitation. The selected region in this case moves eastward along with the propagating MJO waves. An example of this technique is illustrated in Figure 3.7. A MJO event was first identified near 4°S and 57°E in the middle of Indian Ocean on July 4, 2007, where the color change from cold to warm to indicate the time progression. As the wave moves eastward, the strength of the event kept intensifying and started to propagate northward. During its passage over the archipelagos in southeast Asia, the southern part of the wave weakened, and diminished near 135°E. The northern branch ceased on the west side of the international dateline on the August 23 (showing as the warmest color). Each colored dot represents a circular area with a diameter of 2.5° in both longitude and latitude, within which the precipitation measurements from both sensors were averaged.

After re-aligning all 23 events with respect to their individual maximum strength day, mean results for both sensors and the uncertainty field are shown in Figure 3.8. Despite both sensors

having observed the peak precipitation, TMI tends to underestimate the heavy precipitation by 1-2 mm/day during the 3 days before and 3 days after the maximum strength day. The underestimation, however, is not surprising, since TMI is known to have issues with detecting heavy convective precipitation, for the same reason discussed before. Moreover, due to the limited number of available cases, all MJO events were also randomly divided into two groups (one group containing 11 events and the other containing 12 events), and were put through the same analysis as described before. The two groups show qualitatively similar features as in Figure 3.8 (i.e., TMI underestimating the rain rates around the mean peak MJO strength day), which strengthens the robustness of our previous analyses.

The analysis procedure presented here is somewhat uncommon, in that the geographic locations where the uncertainty observations were sampled move along with the MJO centers. The only reason for applying this moving coordinate technique, however, is the lack of high temporal-resolution observations, as it takes nearly 10 days to retrieve a full rainfall uncertainty map over the region of interest. This is much lower than the observational frequency demanded for resolving MJO-impacted uncertainty structures. Hypothetically, given perfectly sampled uncertainty time series (e.g., every 3 hours), there is a good chance that the MJO induced cyclic uncertainties would reveal themselves at time intervals between 30 to 90 days via certain spectral analyses.

3.2.2.3 Seasonal Cycle

The seasonal variation is found to be one of the most robust periodic cycles in the climate system. A grid box is intentionally selected over the west Pacific warm pool (WPWP) to explore the seasonal uncertainty variability.

The precipitation uncertainty over the WPWP contains mostly negative signals within the selected region (Fig. 3.9(a)). TMI overestimates the precipitation during the northern hemisphere winter months (i.e., from December to March of the next year), and the uncertainty sign reverses for the rest of the year (Fig. 3.9(b)). The performances of each sensor in two opposite seasons (winter vs. summer) are shown in Fig. 3.10. The winter months (December, January, and February) are dominated by TMI overestimation (Fig. 3.10(e)), without showing any intensity-dependent preferences. Negative uncertainties (or PR overestimations) dominate the summer rainfall measurements over the same region (Fig. 3.10(f)). This may be attributed to the annual equatorial march and retreat of the sea surface temperature.

3.2.2.4 Multi-Annual Cycle

As one of the most convective regions in the world, the warm moist air across the equatorial central-to-eastern Pacific Ocean rains more than 6 mm/day based on statistical mean values. Interestingly, the measurement differences between TMI and PR are much less prominent (less than 0.5mm/day) near the international dateline, but increase up to 3mm/day towards the east, during which the El Nino Southern Oscillations (ENSO) start to play a more and more important role (Fig. 3.11). A box of 48°×24° in the mid-to-east equatorial Pacific Ocean was chosen to explore the impact of ENSO on the local precipitation uncertainty.

A region of significant TMI overestimations is overlapping with the inter-tropical convergence zone (ITCZ, Fig. 3.11(a)), just a few degrees north of the equator. The monthly precipitation time series from the two sensors are shown in Figure 3.11(b). TMI (blue line) has significantly more rainfall amount than PR (red line), resulting in a severe overestimation of precipitation among the wetter months (black line in Fig. 3.11(b)). Interestingly, the four highest peaks in the uncertainty field (black line) all occur around January (in 2003, 2005, 2007, and

2010, respectively), indicating a possibility of having severe algorithmic defects in characterizing environmental conditions during the northern hemisphere wintertime. Finally, the magnitudes of the uncertainty field seem to oscillate with the monthly mean rain rates, as wetter months tend to produce higher positive uncertainties.

An Empirical Orthogonal Function (EOF) analysis is performed over the monthly precipitation uncertainty time series for the total period of 120 months. Results from the two leading modes (which are the only modes that have passed the significance test) are shown in Figure 3.12. The first EOF mode (Fig. 3.12(a)) shows a clear pulsing signal (i.e., "on and off") over the wettest ITCZ-overlapping rainfall regime. As the pulsing signal implies, wherever it rains, the magnitudes of the precipitation uncertainty are likely to increase accordingly. Since the precipitation uncertainty is defined as the difference between TMI and PR, the pulsing signal also suggests the inclination of having TMI over-reporting rain rates during the wetter months, which supports our arguments and observations from Figure 3.11(b). The corresponding principal component (Fig. 3.12(b)), or the time series of signal intensities, correlates approximately with the ENSO 3.4 Index (red line) from the Climate Prediction Center at the National Weather Service. This suggests a possible link between the ENSO phase change and the precipitation uncertainty variation. In addition, a two-to-three month time lag is observed between the EOF time series and the ENSO index, which might result from the slower oceanic temperature response due to the larger heat capacity of water. The second EOF mode indicates shifting signals between the northern and southern hemisphere (Fig. 3.12(c)), with a mean period close to 12 months (Fig. 3.12(d)). This is likely due to be the residual from the seasonal variability. However, further investigation is needed to confirm this argument.

Overall, the leading two EOF modes could explain a significant portion of the uncertainty variability, indicating a consistent and plausible internal link between the precipitation uncertainty and the ENSO phenomenon over the central-to-eastern Pacific Ocean.

3.2.2.5 Near Constant Biases

The precipitation uncertainty between TMI and PR over the northern Indian Ocean is quite uniform in terms of its geographic variability (Fig. 3.13(a)), where negative biases have filled up most of the grid box. The temporal uncertainty variation (black line, Fig. 3.13(b)), however, seems to contain a large amount of noise, showing as the randomly distributed fluctuations over the time. Surprisingly, for the majority of the timespan, TMI (blue line) is consistently reporting lower rain rates than PR (red line), and the magnitude of the precipitation uncertainty appears insensitive to the monthly mean rain rates.

To further reduce the magnitude of the random noise, monthly climatological precipitation uncertainties (black line, Fig. 3.13(c)) are computed over the 10-year period, together with the TMI (blue line) and PR (red line) measurements. For any given month, the magnitudes of true random uncertainty should have reduced to an insignificant level based upon previous discussions of the random noise propagation.

Both sensors have captured the seasonal variation throughout the year, with wet seasons in the late fall and dry seasons in the early spring. The uncertainty field, however, seems to overlook the seasonal rainfall change, remaining nearly constant with a mean of -0.54 mm/day and a standard deviation of 0.13 mm/day. It is suggested that the prevailing precipitating cloud types over this region may have contributed to the consistent underestimation from TMI (or overestimation from PR). However, without any long-term validation sources, it is not possible to determine which sensor is wrong. Hopefully, with the launch of the GPM satellite, better-

constrained cloud microphysics information can be retrieved from the Dual-Frequency Precipitation Radar, and thus help to investigate the reason behind the consistent underestimation by the radiometer over this region.

CHAPTER 4

DISCUSSION

The forward model, which includes the simulation of atmospheric conditions as well as radiative transfer calculation, was identified in Stephens and Kummerow (2007) to contribute a substantial portion of the total precipitation uncertainty via inappropriate and inaccurate microphysical assumptions. Because of the physical connections between the microphysical parameters and atmospheric regimes, the forward model uncertainties are rarely constant but tied to atmospheric cycles, as shown in Chapter 3.

The first section of Chapter 4 will use precipitation measurements over a pre-defined region to explore how different regional atmospheric cycles influence the uncertainty structures and how different uncertainty sources contribute to the total precipitation uncertainty. The remainder of the chapter will then show the variations of precipitation uncertainty partitions for a variety of sampling resolutions, focusing on the propagation of major uncertainty sources in both time and space. Finally, a similar uncertainty analysis is applied to a different tropical ocean basin to highlight regional discrepancies in the uncertainty structures.

4.1 Spectral Analyses of Precipitation Uncertainty

The precipitation data are taken from 5-day averaged surface rain rates over the central Pacific (161°W~157°W, 8°N~4°N), for both TMI and PR, from Jan 2002 to Dec 2011. The temporal series of the precipitation uncertainty (defined as TMI minus PR) is passed through a low-pass filter to reduce noise. Results are shown in Figure 4.1(a). A fast Fourier transformation is then applied to the smoothed uncertainty time series, resulting in four statistically significant spectral peaks (labeled A-D in Figure 4.1(b)).

The most substantial atmospheric cycle (peak B), which exceeds the 95% confidence limit, peaks at 10 cycles per 10-year period, indicating the presence of annual variability (also known as the seasonal cycle). The variations are thought to be associated with the annual meridional movements of the ITCZ, as shown in Figure 4.2. It is speculated that the precipitation uncertainty may be involved with the height of convective organization and the meridional migration across the ITCZ from the southern border of the box (4°N) to the northern border (8°N) on an annual basis. Besides the annual variation, there are three other spectral peaks with greater than the 90% confidence, namely the 18-month peak (6 cycles per 10-year period, peak A), 6-month peak (20 cycles per 10-year period, peak C), and 135-day peak (27 cycles per 10-year period, peak D). Peak A is likely associated with the ENSO phenomenon, in that the 10-year ENSO 3.4 indices have disclosed an ENSO phase period between 16-20 months (i.e., there are a total of seven ENSO cycles over 120 months, as shown in Fig. 3.12(b)), which could be readily aliased into this 18-month uncertainty spectral peak. Peak C is possibly associated with the meridional solar movement, as the sun crosses the area of interest approximately every 6 months. The physical reasons that result in peak D are more complicated, as there are two possible explanations for the spectral peak. The first possibility is mechanical and comes from TRMM's 46-day orbiting repeat cycle. The extent to which the 46-day sampling strategy could have impacted the uncertainty pattern, however, is not clear at this moment and requires further studies. On the other hand, the 135-day peak could also have indicated the presence of diurnal cycles in the uncertainty field, as the diurnal cycle is now being sampled every 46 days and the diurnal signals could be aliased into the 135-day peak. Further investigations (see Fig. 4.3) seem to confirm the second speculation, as there is clear evidence of having strong diurnal uncertainty cycles over this particular region.

To retrieve more climatologically stable results, a broader region over the same meteorological regime (144°W~120°W, 3°N~9°N) was chosen to perform the same spectral analysis (see Fig.4.4). In addition, the overall monthly precipitation uncertainties will be presented by a collection of individual contributions from major uncertainty sources (Fig.4.5), where a spatial resolution of 3°×3° has been chosen to complete the analysis with an acceptable noise level. In comparison to Figure 4.1, the 135-day spectral peak, which is considered to be driven by the diurnal cycle, has disappeared from the current analysis. This could be associated with the smoothing effect from averaging uncertainty data across multiple time zones. At the same time, the strength of the 6-month peak has been reinforced, possibly due to the zonal-oriented placement of the rectangular research box (i.e., the east-to-west length of the box is 3 times longer than the south-to-north width, which may result in amplification of meridional disparities). However, the relative contribution from the 6-month peak has failed to pass the significance test from the EOF analysis; hence, it is not considered as an independent major uncertainty source.

When calculating the major uncertainty sources, the random uncertainty percentage is calculated from the pixel uncertainty itself, and the constant bias contribution is evaluated from the 10-year (2002-2011) surface rain rates differences between TMI and PR, whose values are the same as in Figure 3.3. Two major atmospheric cycles are identified to have substantial impacts on the rainfall uncertainty field – the seasonal cycle and the El Nino Southern Oscillation (ENSO). In addition, contributions associated with the regional atmospheric cycles are estimated from the principal components of the EOF analyses, during which only constant biases (instead of seasonal variations) were removed before applying the EOF method.

The largest contribution to the overall precipitation uncertainty comes from the constant biases, which accounts for over 55% of the total uncertainty. The random uncertainty, in

contrast, only explains approximately 2% of the month-to-month variability. Within the remaining 43% of uncertainty, ENSO phenomenon explains over 30% (or 13% of the overall uncertainty) and the seasonal variation is associated with another 17% (or 7% in the overall) of the uncertainty. A quarter (~22.5%) of the overall uncertainty cannot be properly explained by the hypothesis proposed at the end of Chapter 1 (i.e., a large portion of un-explained precipitation uncertainty should consist of multiple cyclic patterns). It nonetheless reduces the un-explained uncertainty by 68%, compared to the original 44% un-explained precipitation uncertainty (see Fig. 3.4 for original uncertainty partitions).

4.2 Qualitative Precipitation Uncertainty Partitions

Over the same region as in Figure 4.5, the major precipitation uncertainty sources are now examined for different temporal and spatial resolutions (Fig. 4.6). To simplify the discussion, the impacts due to changing temporal resolutions are discussed first, followed by the spatial resolution. A similar uncertainty analysis will be performed over the eastern equatorial Atlantic, with the intent of highlighting regional discrepancies.

The time series of the precipitation uncertainty measurements have been integrated over 1 and 3 months, respectively, for both 1°×1° and 3°×3° spatial resolutions. The random uncertainty percentages decrease as more and more Gaussian-distributed noise is averaged to zero. The precipitation uncertainty due to constant bias, in contrast, gains in relative importance, in that the similarity level between the sampled uncertainty and the 10-year constant bias increases with longer sampling period. For a hypothetical extreme case, in which the sampling period is the same as the length of the uncertainty database (i.e., 10 years), the sampled uncertainty is the same as the constant bias, and the constant bias should therefore explain 100% of the overall

uncertainty. Meanwhile, there are also substantial uncertainty percentage increases associated with the regional atmospheric cycles – either by the seasonal cycle or by the ENSO phenomenon.

Aside from corresponding to the two relatively well-known long-term cycles, a portion of the overall precipitation uncertainty should also be influenced by other coincident but not easily identifiable cycles, especially near the short-term end, such as the impact from diurnal cycle. The sampling strategy of the TRMM satellite, however, limits its ability to resolve impacts from short-term cycles, as it takes the sensors approximately 10 days to complete one full scan over the region of interest, unless special treatments (like the "moving coordinate" technique from Chapter 3) are applied to the dataset. Despite the lack of high temporal-resolution uncertainty data, the relative importance of random noise should increase on shorter time scale, with decreasing percentages associated with constant bias and regional atmospheric cycles.

The impacts due to changing spatial resolutions are qualitatively similar to the temporal-resolution effect. With larger grid boxes, the random noise explains less variability, while the constant bias and regional atmospheric cycles now have greater influence on the overall uncertainty. With the coarsest data resolution (3°×3°, 3-month integration), the percentage of un-explained uncertainty drops to 14%, which is only 40% of the un-explained uncertainty at the highest data resolution (1°×1°, 1-month integration).

For any of those four scenarios, there is always a certain level of unknown uncertainty (the magenta shaded regions in Fig.4.6) that cannot be properly explained by the proposed classification scheme, ranging from 14% to 35% of the overall uncertainty. As suggested earlier, part of the unknown uncertainty could result from the short-term atmospheric cycles that are not resolvable using sporadically sampled data, or any localized weather phenomena that are too small for the pre-defined box sizes. Another possible cause of the unknown uncertainty stems from inappropriately interpolating the mesoscale precipitating systems (ranging from tens of

kilometers to hundreds of kilometers in horizontal directions) into pre-defined grid boxes. During the interpolation, the original 2-D rainfall uncertainty field (which may correspond well to the regional precipitating cycle) was broken into multiple boxes and analyzed individually. Hence, the connection between each grid box and the precipitating cycle has been attenuated, and thus explains less uncertainty variability. Finally, the random uncertainty group includes a majority of random noise, but not all of it. For the excluded random processes, it is speculated that they could have finite contributions to the total un-explained uncertainties.

Similar tests have been carried in the eastern equatorial Atlantic (27°W~12°W, 9°N~3°S) in order to illustrate the regional differences in the uncertainty source partitions. Only two spectral peaks have been identified as significant uncertainty cycles (see Fig. 4.7), namely the annual (Peak B) and semi-annual (Peak C) cycle. Further investigations using the EOF analysis (Fig. 4.8) have shown that the leading two modes are both indicating a 12-month variability (pulsing signal vs. shifting signal, see Fig. 4.8.(a) and (c)), while the principal components from the two modes are shifted by approximately 6 month (Fig.4.8.(b) and (d)), which may help to partially explain the existence of the 6-month spectral peak. To be conservative, only the relative contributions from the leading mode will be considered as the annual uncertainty variability.

Despite negative constant biases being frequently observed over this region (Fig. 4.9), it only helps to explain approximately 20% of the overall precipitation uncertainty, except for the lowest data resolution (~32%). The random noise percentages, which vary from 5 to 11%, are nearly twice as much as those in the central Pacific, indicating a smoother probability distribution of hydrometeor profiles in terms of their surface rain rates. Instead of being influenced by two locally dominant atmospheric cycles (i.e., the seasonal variation and ENSO), the cyclic portion of the precipitation uncertainty over the eastern Atlantic is mostly affected by the season variation alone. Although there are studies demonstrating the ENSO tele-connections between

the central Pacific and eastern Atlantic (Giannini et al. 2001), the ENSO impact does not reveal itself as a major uncertainty signal. A physical connection in the actual precipitation field cannot necessarily guarantee a successful transfer into the uncertainty field, as the later is more related to the empirical and artificial model assumptions rather than the actual rainfall amount. Mathematically, the hypothesized cyclic uncertainty pattern helps to reduce the original unknown uncertainty substantially, leaving the final un-explained uncertainty at 27% (at the lowest data resolution), which corresponds to more than 63% of relative improvement.

CHAPTER 5

CONCLUSION

Precipitation retrieved from space-borne microwave radiometers has been providing invaluable information about global precipitation information since early 1970s; the associated measurement uncertainty, on the other hand, has been overlooked until recently. Many studies mentioned in the introductory chapter have identified the spatial and temporal variability of the precipitation uncertainty, mostly as a consequence of inappropriate and inaccurate microphysical assumptions of the precipitating environment in the forward model. A few uncertainty-predicting models that were recently developed have tried to incorporate more spatial and temporal structures to account for the variability (Adler et al. 2012; Maggioni et al. 2014). The essence of the variability, or the internal structure of the uncertainty, remains elusive.

By comparing precipitation products measured by two collocated but nearly independent sensors aboard the TRMM satellite (i.e., TMI and PR), this study provides insight into the internal structures of the satellite-retrieved precipitation uncertainty. Preliminary results have shown that the precipitation uncertainty can be largely divided into stochastic and systematic components. Moreover, for either component, a number of uncertainty sources have been identified to contribute cooperatively to the final uncertainty. Stochastic uncertainty can be expressed mathematically as Gaussian-distributed noise, and the magnitude of variability decreases quickly with averaging of data. The systematic uncertainty, in contrast, can be further decomposed into the region-dependent constant biases and localized cyclic patterns that vary with space and time. Among multiple sources that may have caused the cyclic patterns, inappropriate and inaccurate atmospheric parameterizations in the forward model (including the cloud-resolving model and radiative transfer scheme) are expected to have the largest impact on

the total uncertainty pattern. This is due to the fact that many key cloud parameters in the model, such as the cloud ice density and drop size distributions, are assigned with empirically derived values regardless of their spatial and temporal variability.

Further investigations from this study have shown that there is a hierarchy of atmospheric cycles that have impacted the precipitation uncertainty structures over major tropical oceanic basins, ranging from the diurnal cycle to seasonal variation, and eventually to multi-annual oscillation. Despite multiple atmospheric cycles exerting influences simultaneously on the local precipitation uncertainty field, the major uncertainty variability is usually dominated by the leading one or two cycles. For different basins, nonetheless, the leading cycles may differ. Besides the actual physical reason (i.e., the atmospheric cycles) that contributes toward the regional cyclic pattern, the uncertainty analyses are largely subject to the change of sampling resolution, in both space and time. In general, uncertainty percentage explained by the random source decreases with lower sampling resolution (via either longer integrating time periods or larger grid boxes), while uncertainty percentages related to constant biases and localized atmospheric cycles tend to increase correspondingly. Through a number of sensitivity tests, it is clear that data resolution changes only the magnitudes of uncertainty percentage that can be explained by individual source, leaving the major properties associated with any given uncertainty source unchanged. Eventually, qualitative uncertainty partitions have shown that with an appropriate choice of sampling resolution, the proposed hypothesis in this study can help reduce the ill-explained portion of the total precipitation uncertainty up to 68 percent.

Going forward, the construction of a dynamic precipitation uncertainty prediction model should be carefully considered and proposed, which include the uncertainty predictions for both stochastic and systematic uncertainties. The former part requires the quantification of the relative importance contributed by major random uncertainty sources, which include but are in no way

limited to instrument noise and sampling errors. Statistical laws and theories may be used to simulate the temporal/spatial propagations of these random uncertainties. The mathematical realizations for the systematic uncertainty, on the other hand, can be much more complicated, especially for those introduced by the forward model, as they require actual physical understanding of the reason that have caused the model to generate the biased results.

Irrespective of the difficulties mentioned above, the benefits of having an uncertainty database for the radiometer-retrieved precipitation products would be tremendous. The uncertainty database would potentially expand the extent to which the space-measured precipitation products can be trusted and utilized in the future. A variety of atmospheric applications, such as the quantification the precipitation-induced latent heat release associated with the global energy equilibrium, the prediction of regional hydrological balance in support of water source management, and the validation of numerical weather prediction, could all utilize the improved precipitation uncertainty estimates.

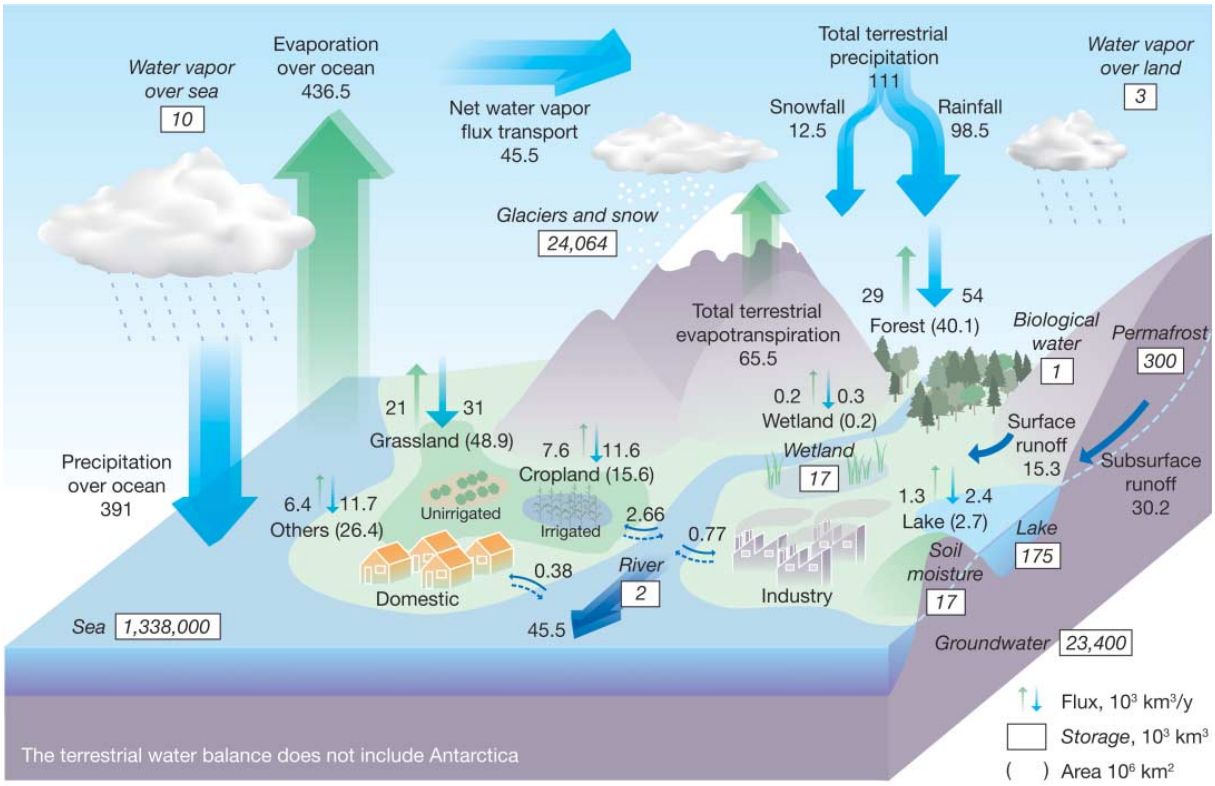

Figure 1.1 Schematic Hydrological Cycle (Oki and Kanae, 2006)

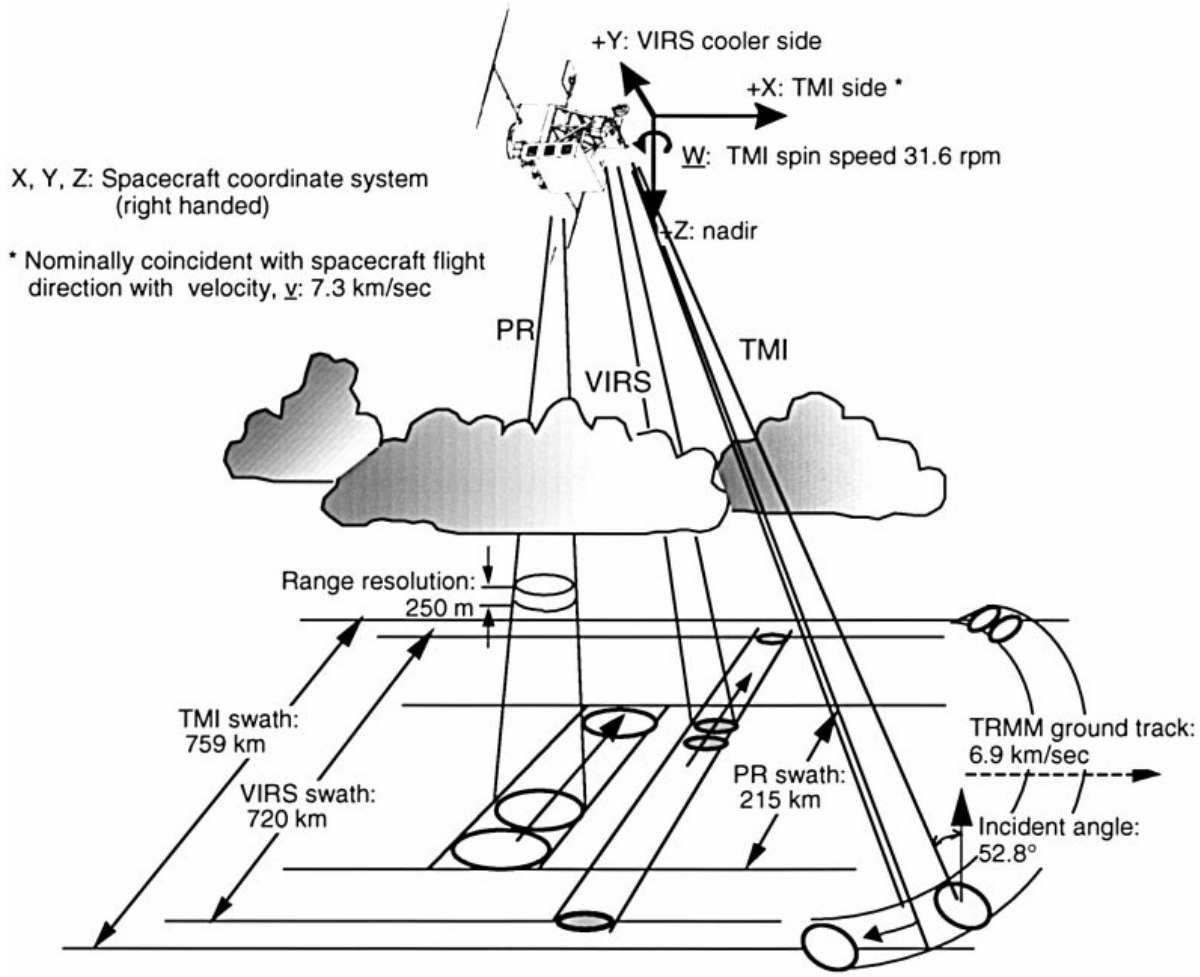

Figure 2.1 TRMM Scanning Geometry (Kummerow et al. 1998)

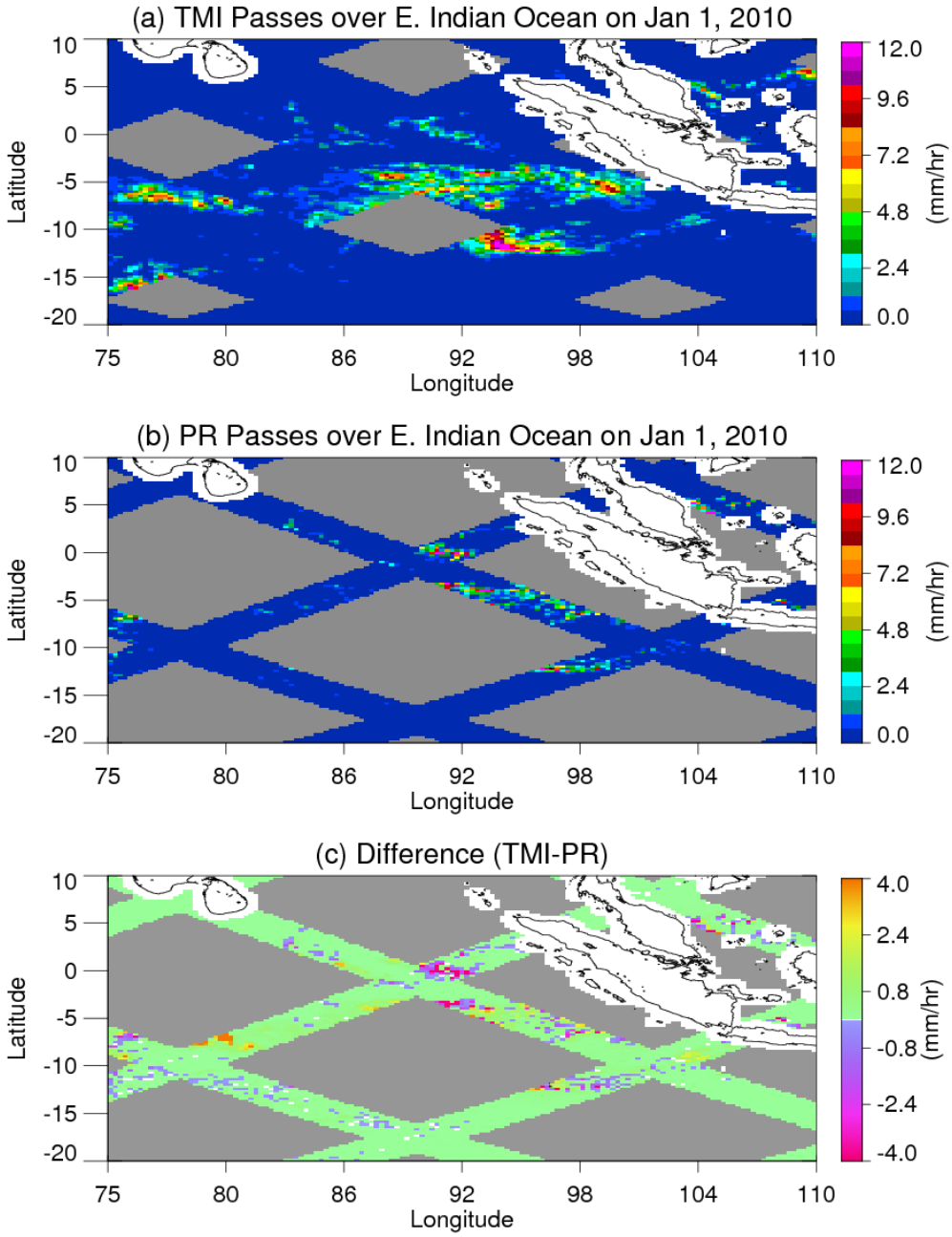

Fig. 2.2 A Snapshot of Surface Precipitation Retrieved from (a) TMI, (b) PR, and (c) the difference between TMI and PR on January 1, 2010

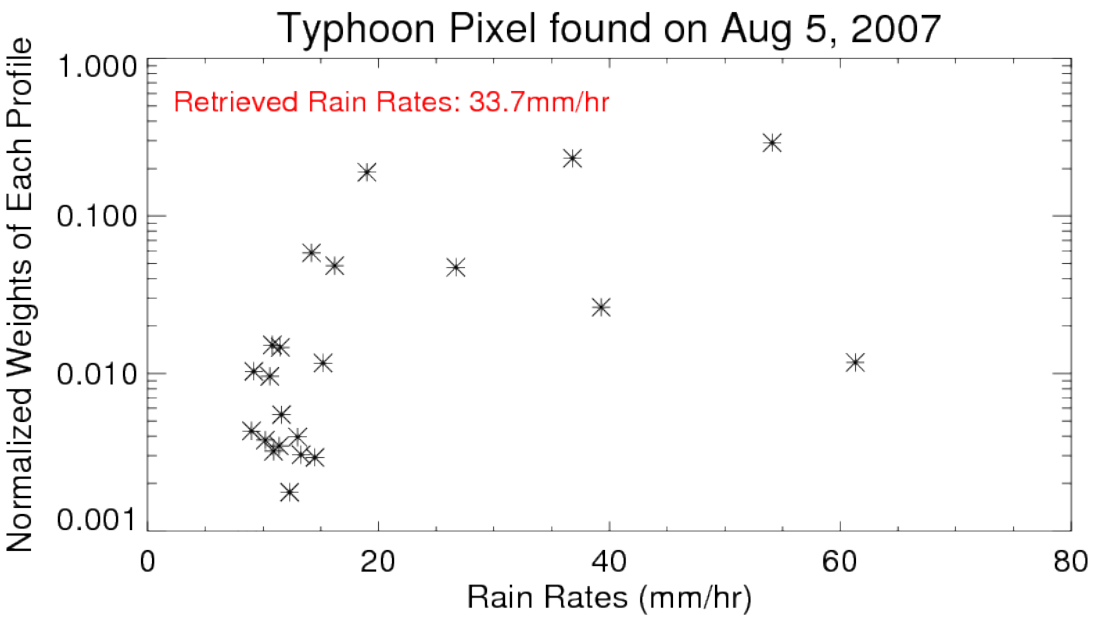

Figure 3.1 Normalized Weights of 22 Most Important Hydrometeor Profiles Selected for A Typhoon Pixel Raining at 33.7 mm/hr over Eastern China Sea on August 5, 2007

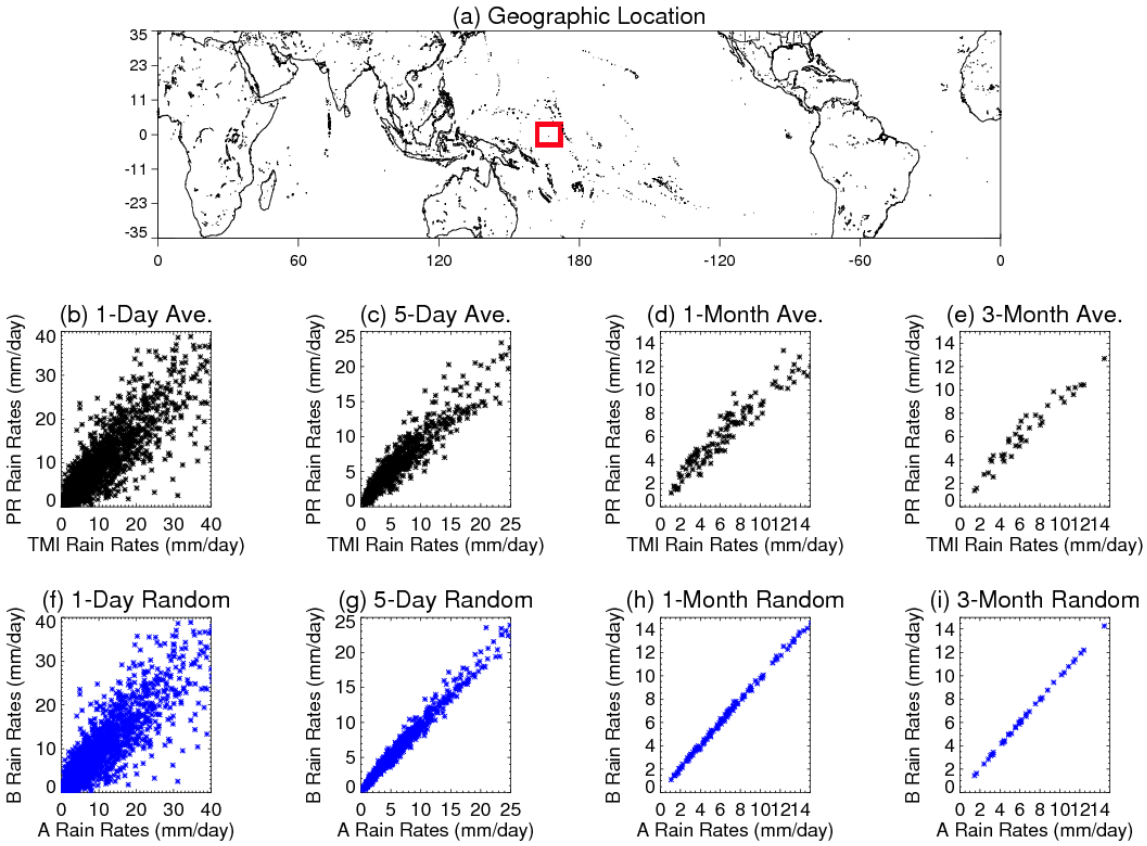

Figure 3.2 Scatter Plot of TMI and PR Surface Rain Rates in A 10°×10° Grid Box Over the Western Pacific, from Jan 2002 to Dec 2011

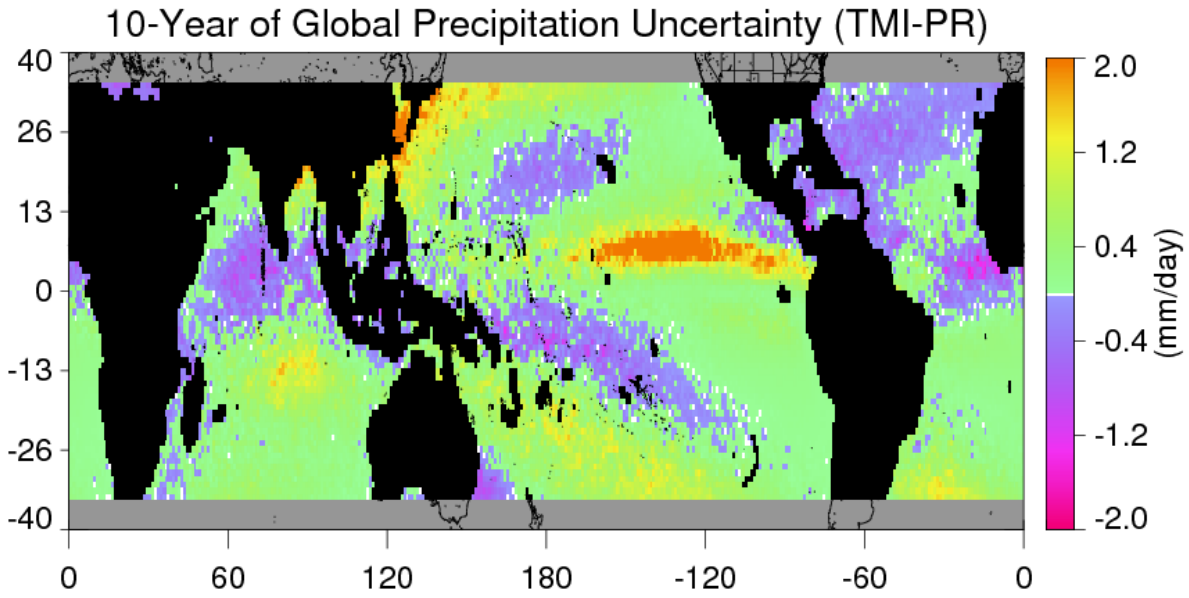

Figure 3.3 10-Year Surface Precipitation Difference Between TMI and PR

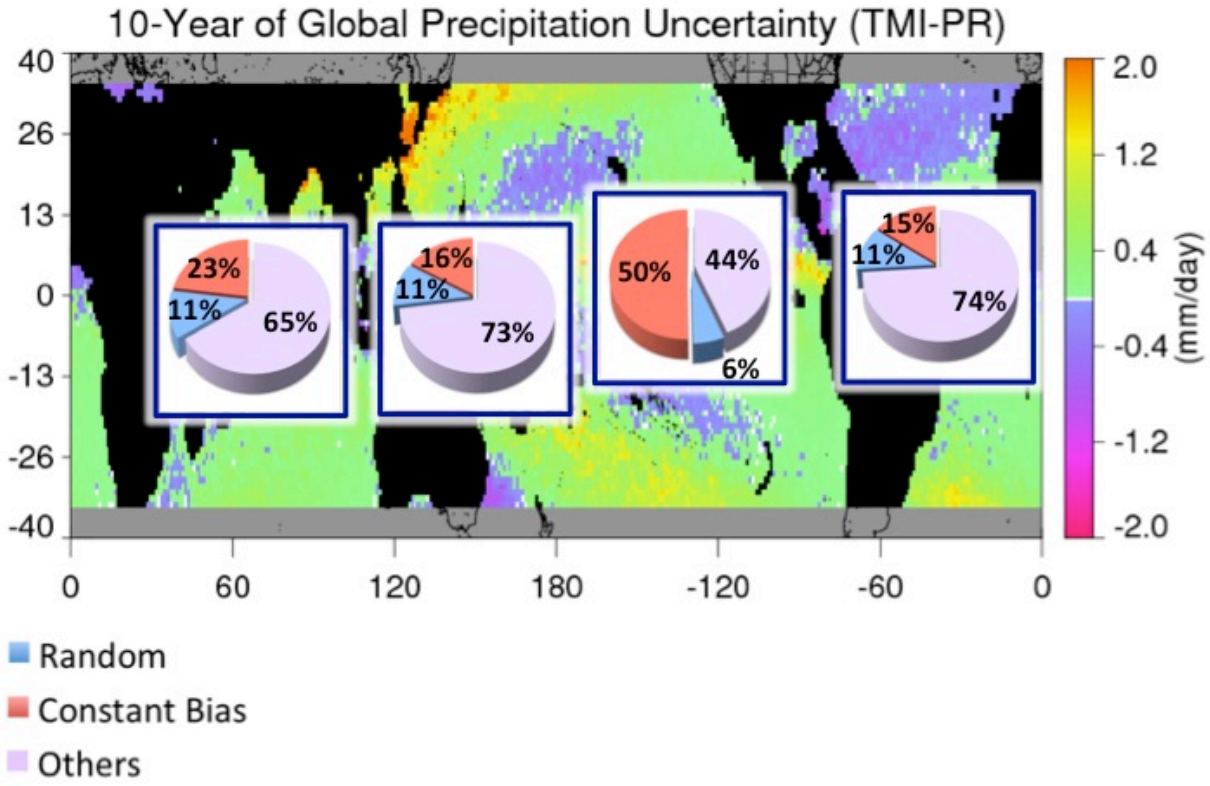

Figure 3.4 Random, Constant Bias, and Other Uncertainty Source Partitions over Four Tropical Ocean Basins

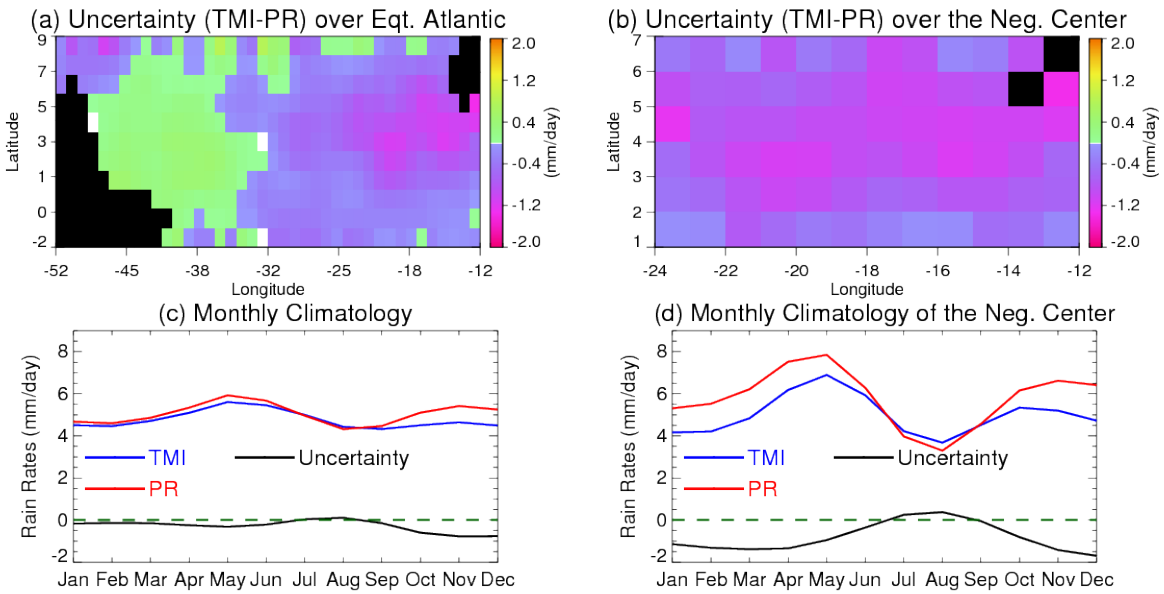

Figure 3.5 An example of undesired vs. desired box choosing over the eastern equatorial Atlantic

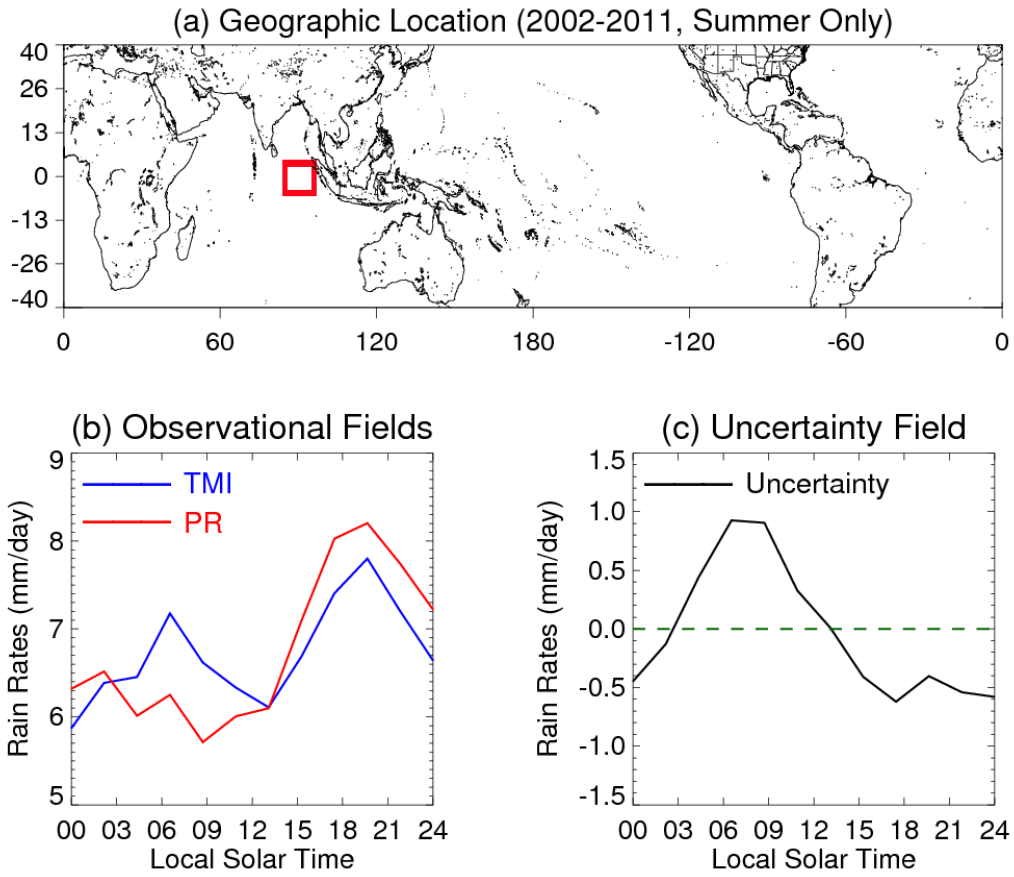

Figure 3.6 Diurnal Uncertainty Variability

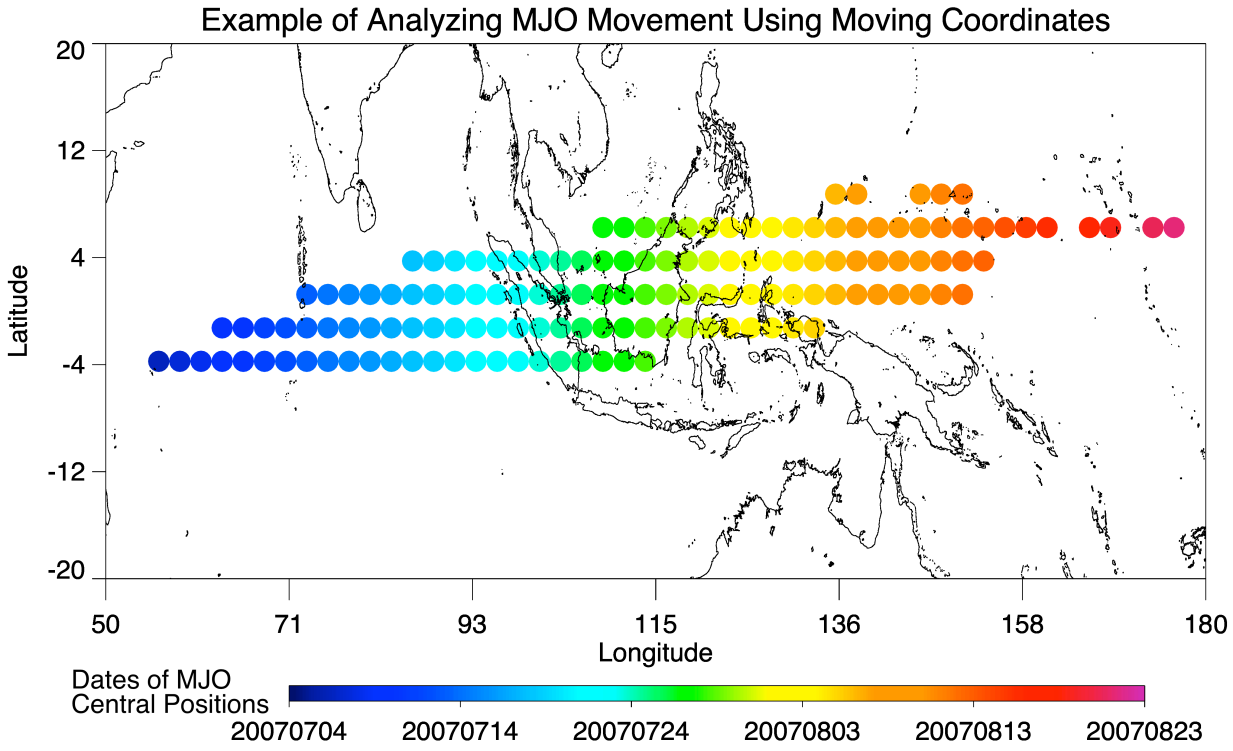

Figure 3.7 Illustration of the Moving Coordinate Technique to Trace a MJO Event

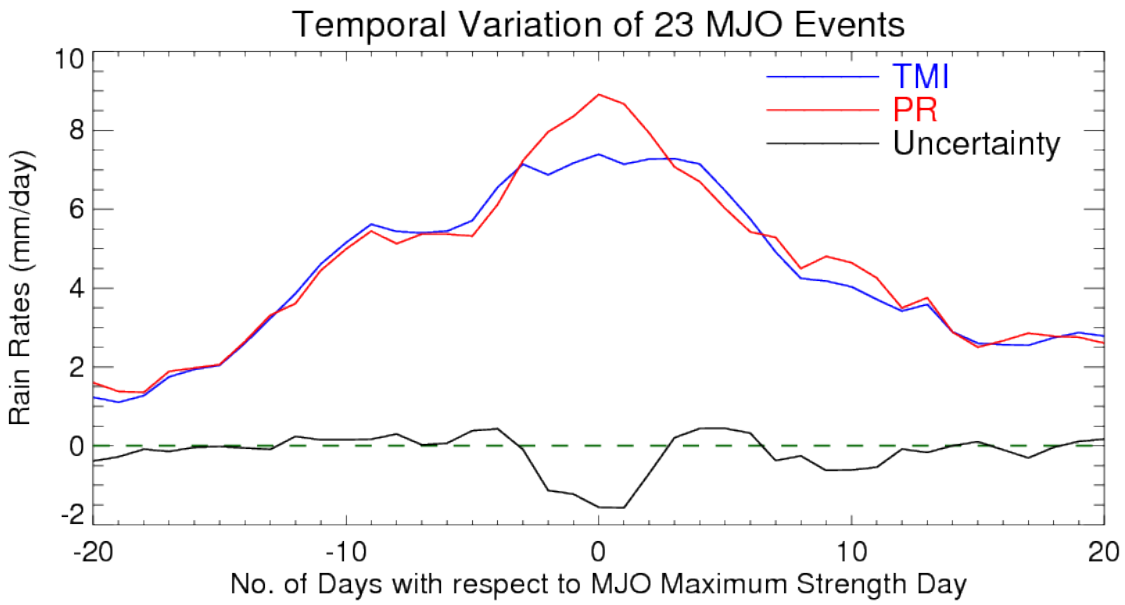

Figure 3.8 Uncertainty Cycle Associated with MJO Events

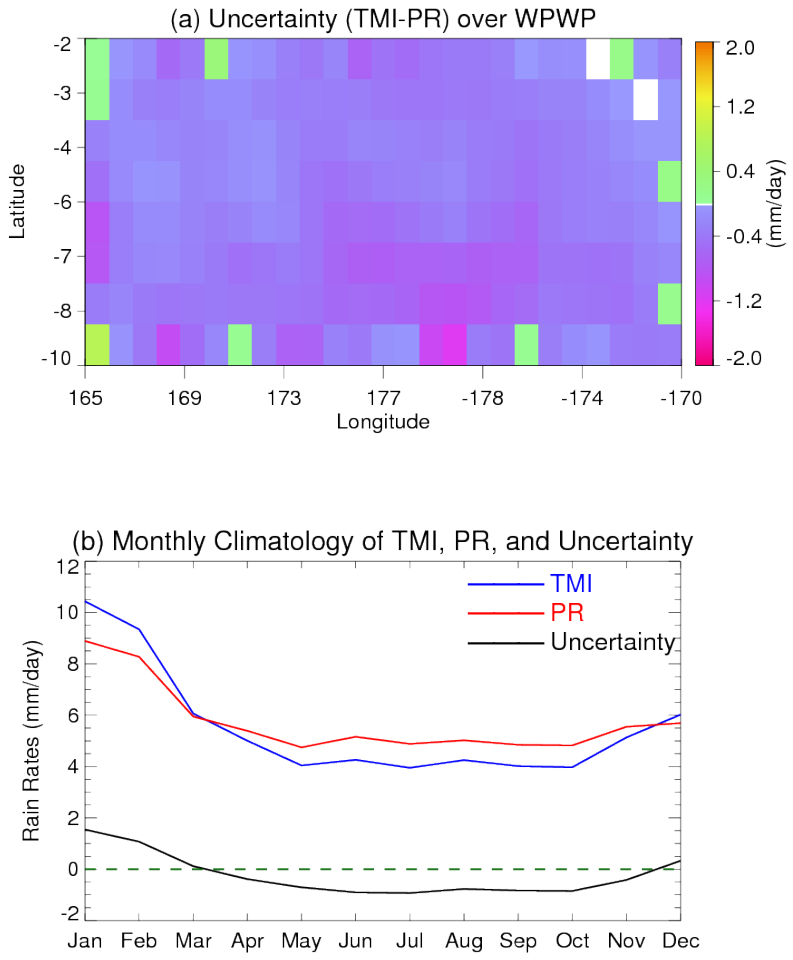

Figure 3.9 Seasonal Uncertainty Variability over the West Pacific Warm Pool

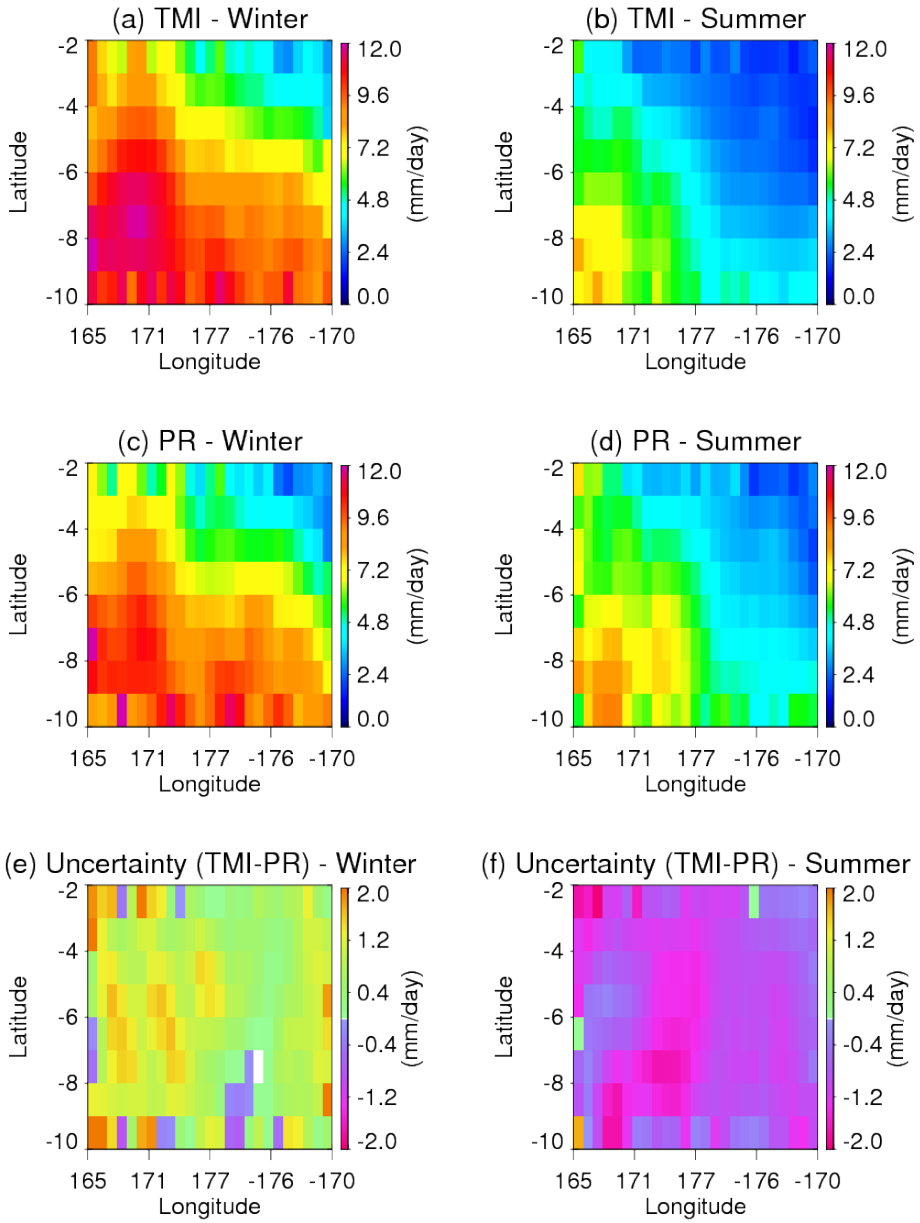

Figure 3.10 TMI, PR, and Uncertainty Field over the West Pacific Warm Pool over Winter and Summer Seasons, respectively

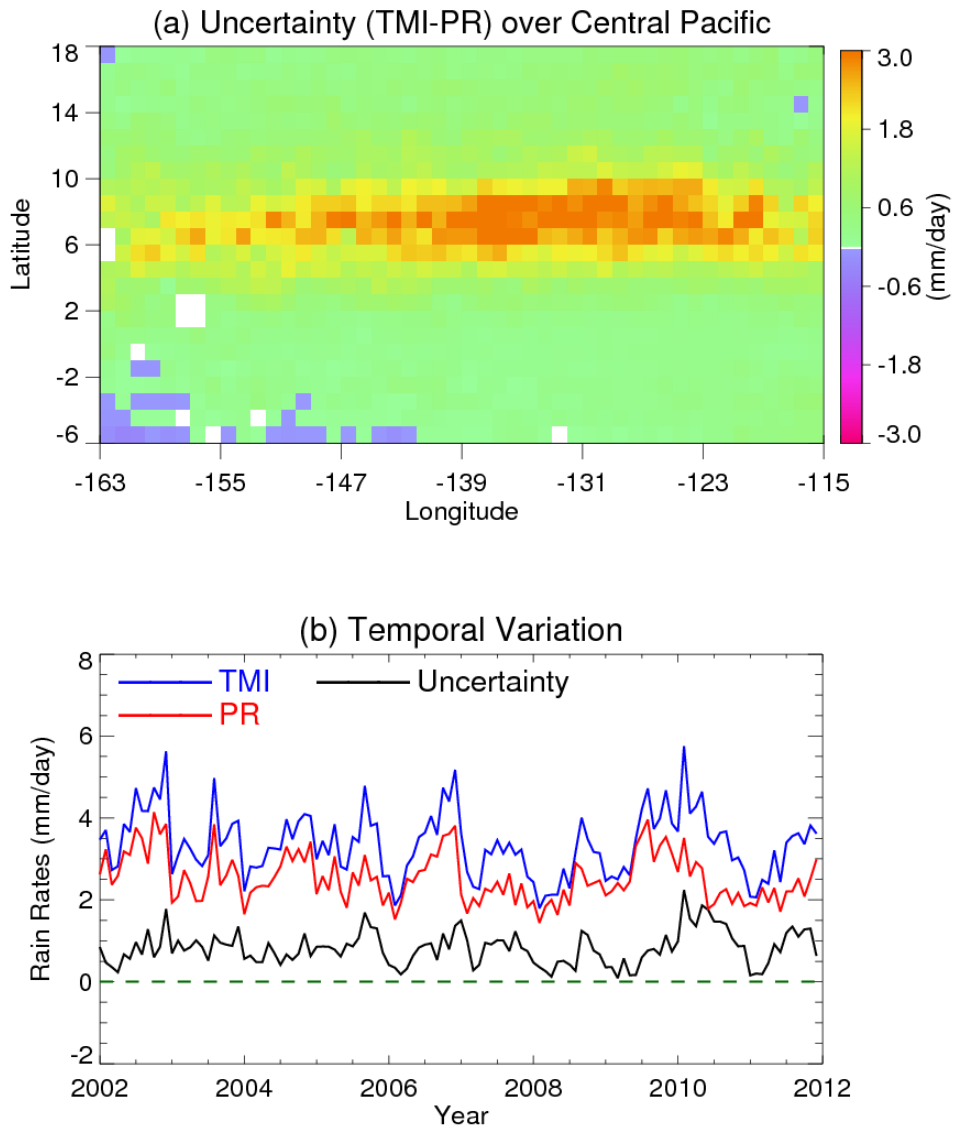

Figure 3.11 Multi-Annual Uncertainty Variability over the Central-to-Eastern Equatorial Pacific

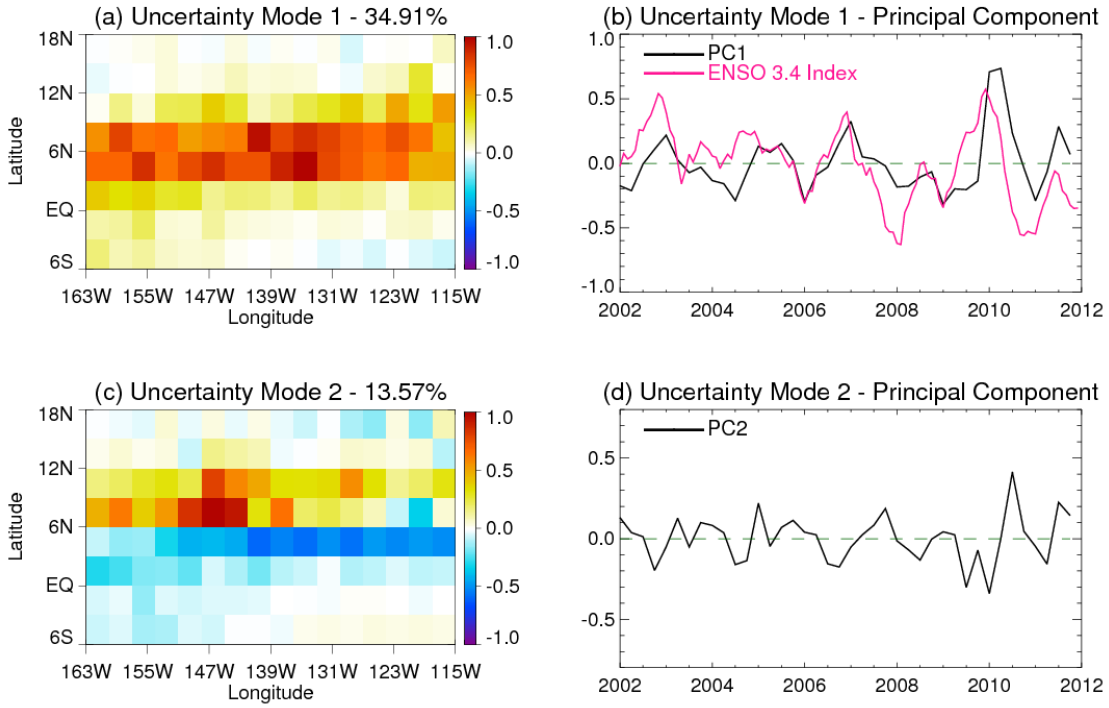

Figure 3.12 EOF Analysis of Uncertainty Fields over the Central-to-Eastern Equatorial Pacific

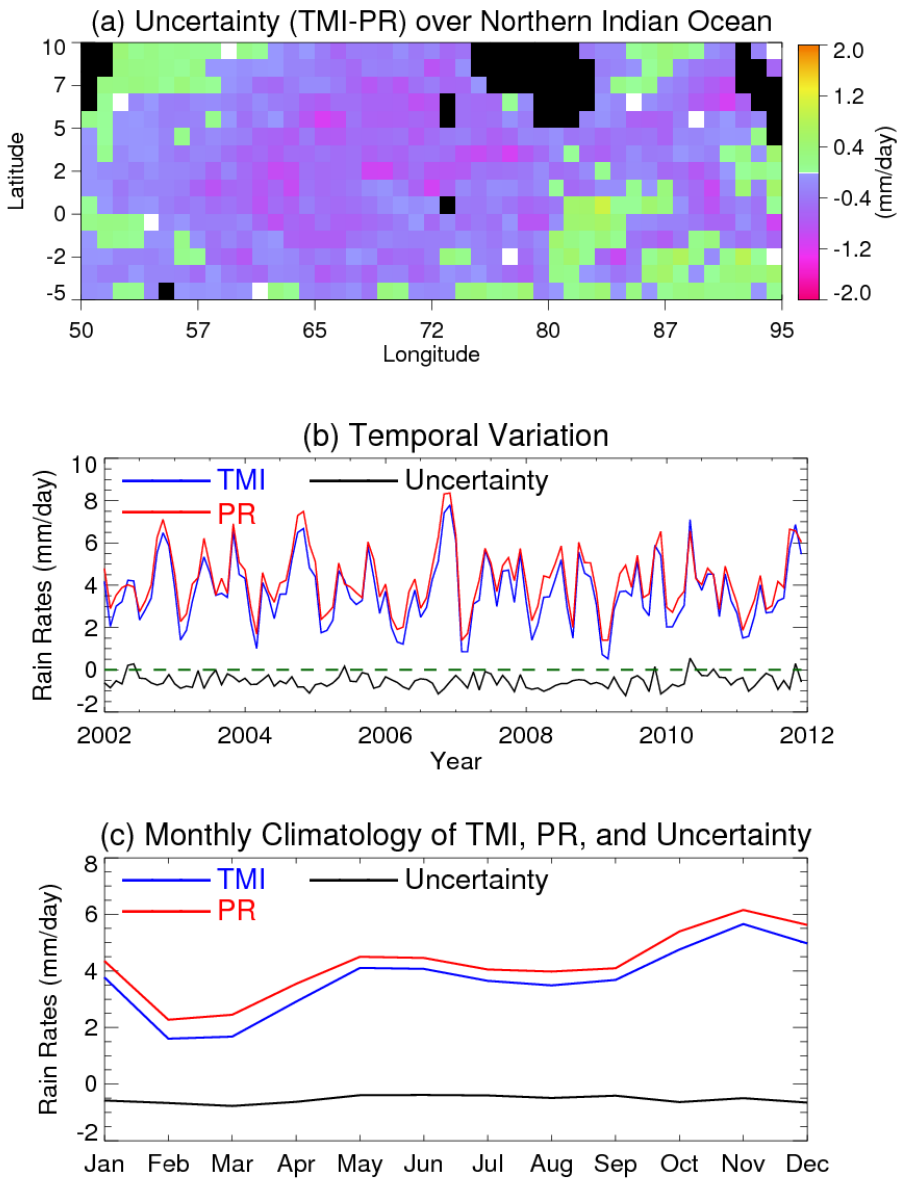

Figure 3.13 Near Constant Uncertainty Cycle over the Northern Indian Ocean

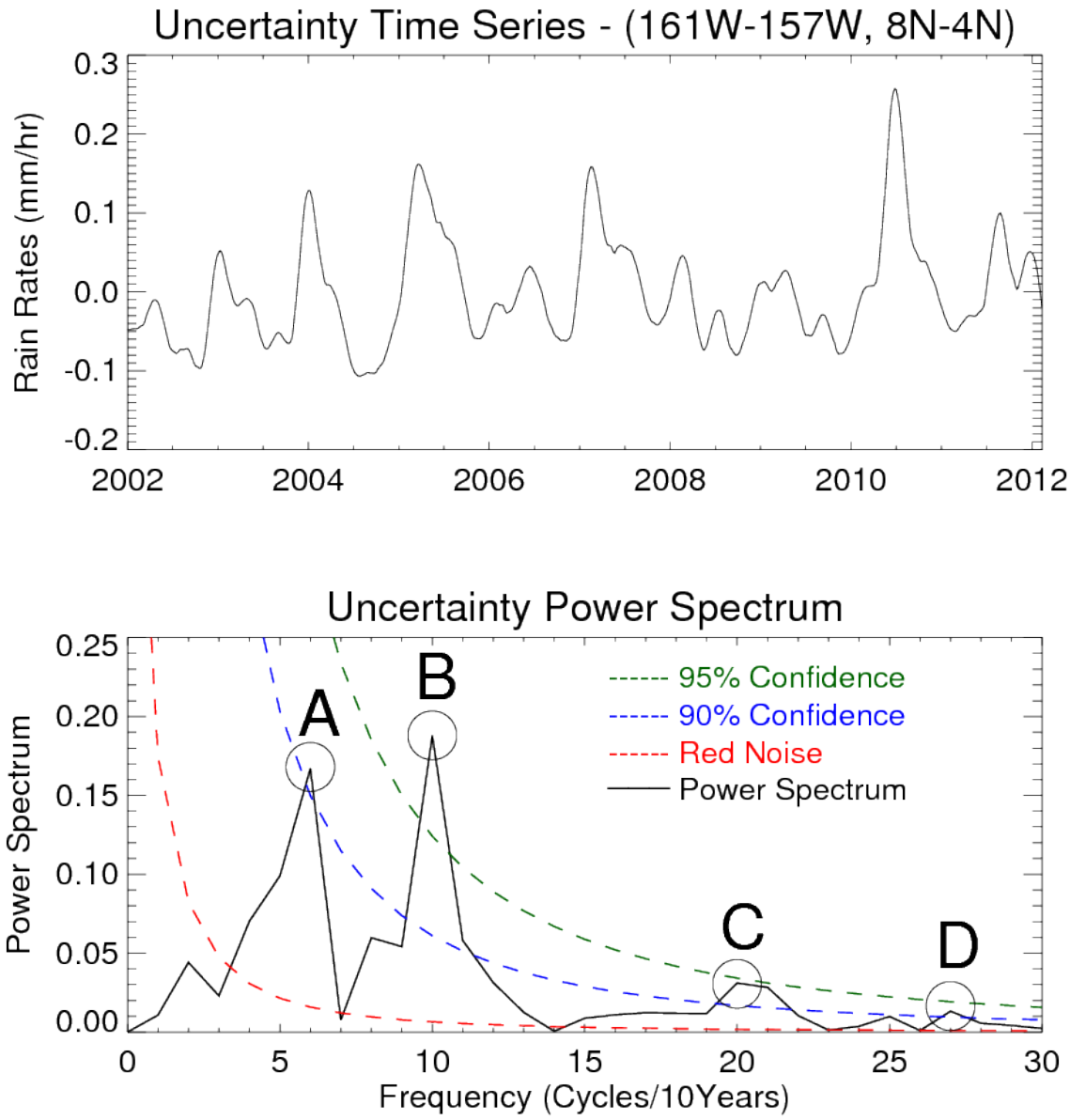

Figure 4.1 FFT Analysis on the Uncertainty Field of a 4°×4° Grid Box over Central Pacific

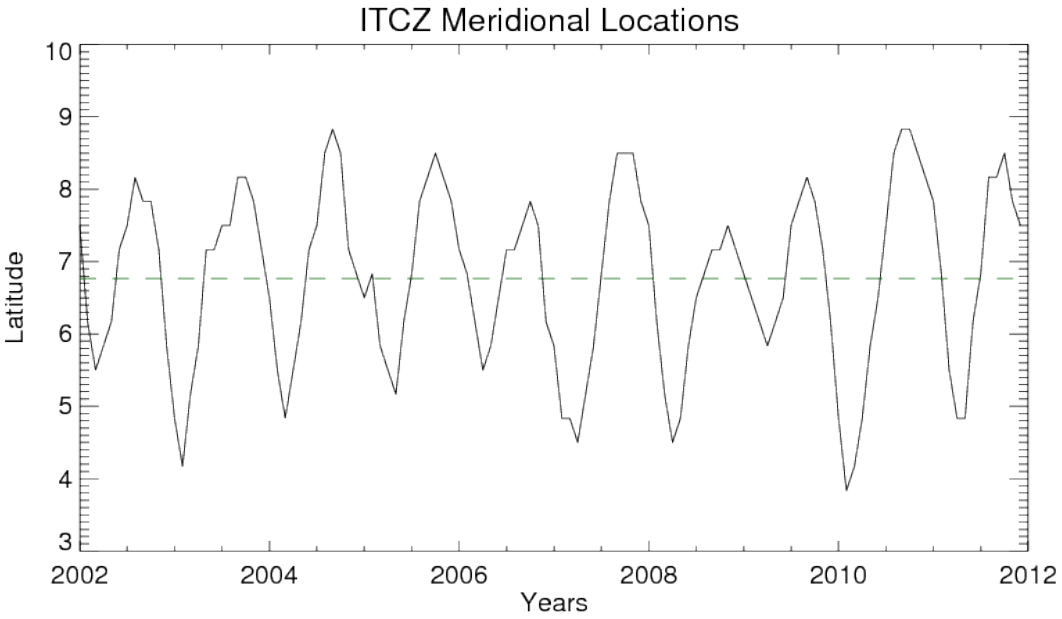

Figure 4.2 Annual Meridional Movements of the Central ITCZ Locations

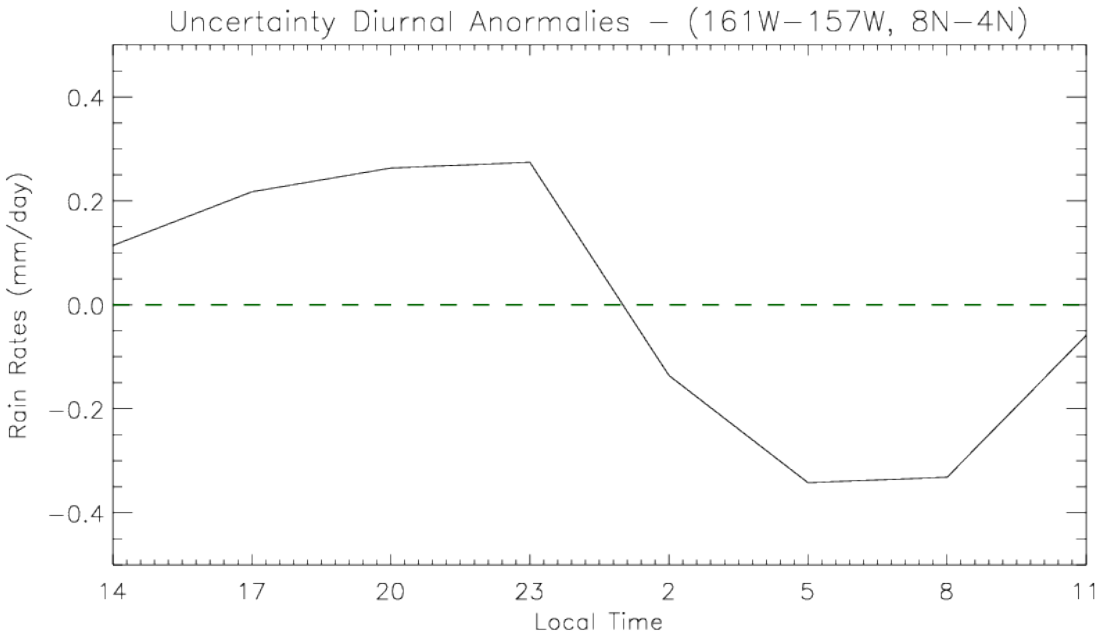

Figure 4.3 Diurnal Uncertainty Cycle over a 4°×4° Grid Box over Central Pacific (TMI-PR)

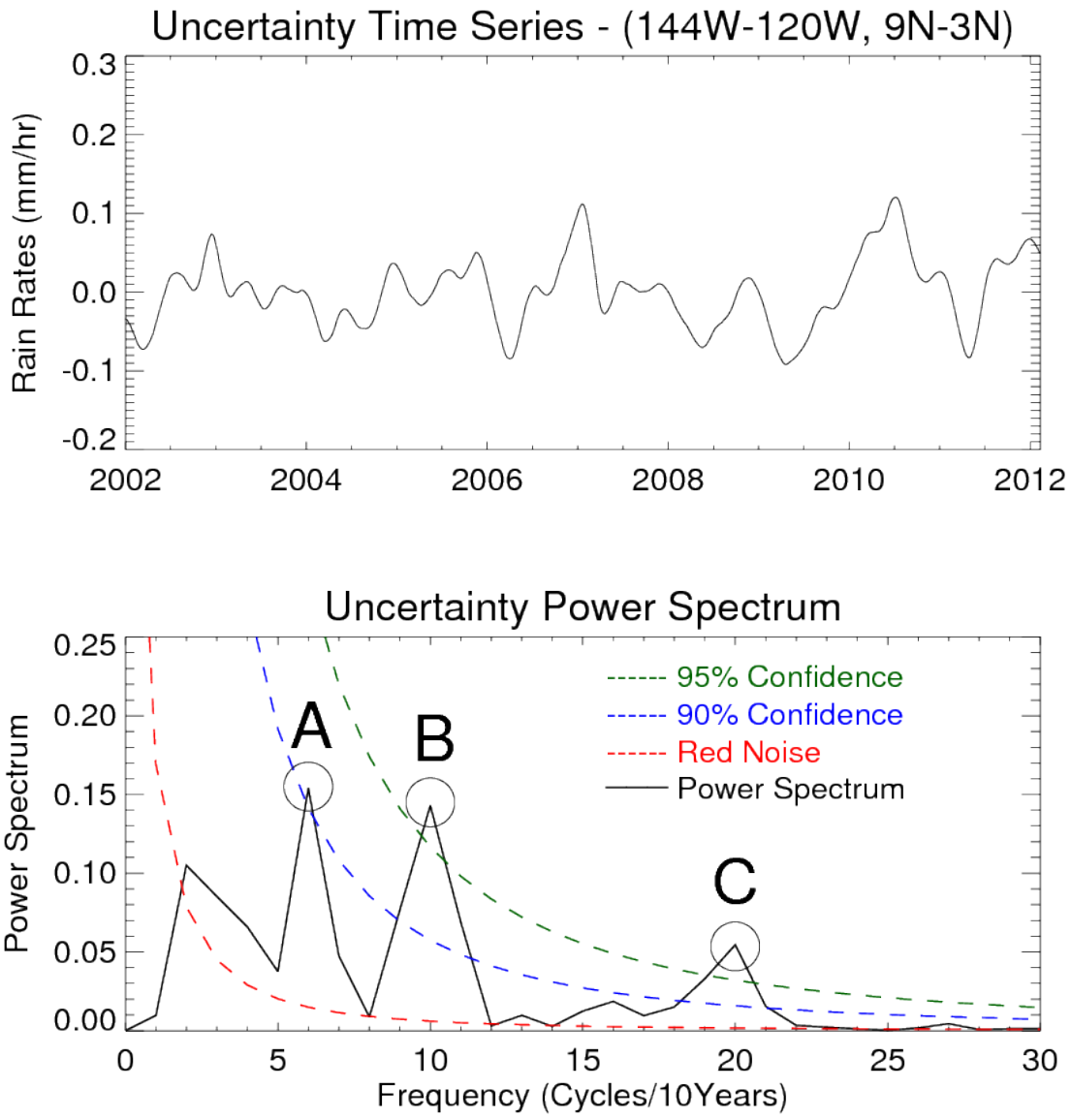

Figure 4.4 FFT Analyses over the Central-to-Eastern Equatorial Pacific

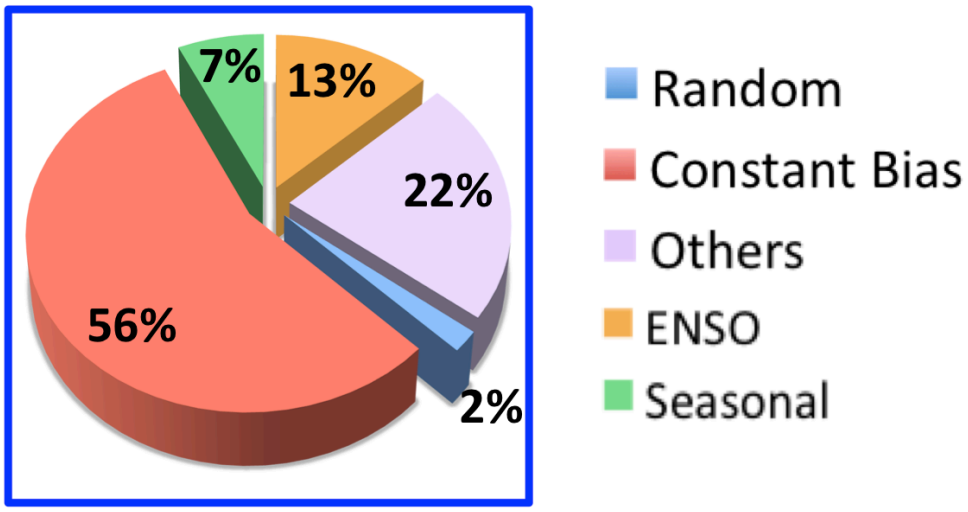

Figure 4.5 Major Uncertainty Source Partitions over the Central-to-Eastern Equatorial Pacific

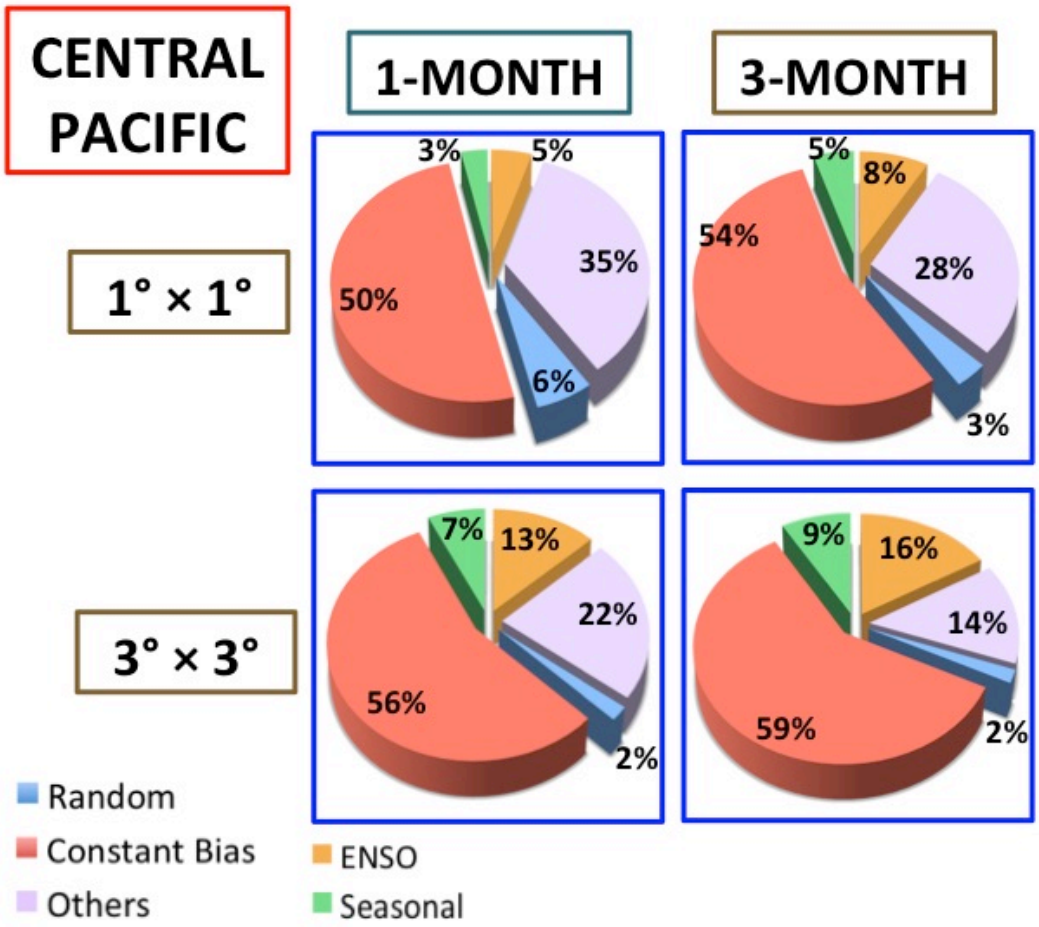

Figure 4.6 Major Uncertainty Sources Partitions over the Central-to-Eastern Equatorial Pacific under Various Spatial and Temporal Resolutions

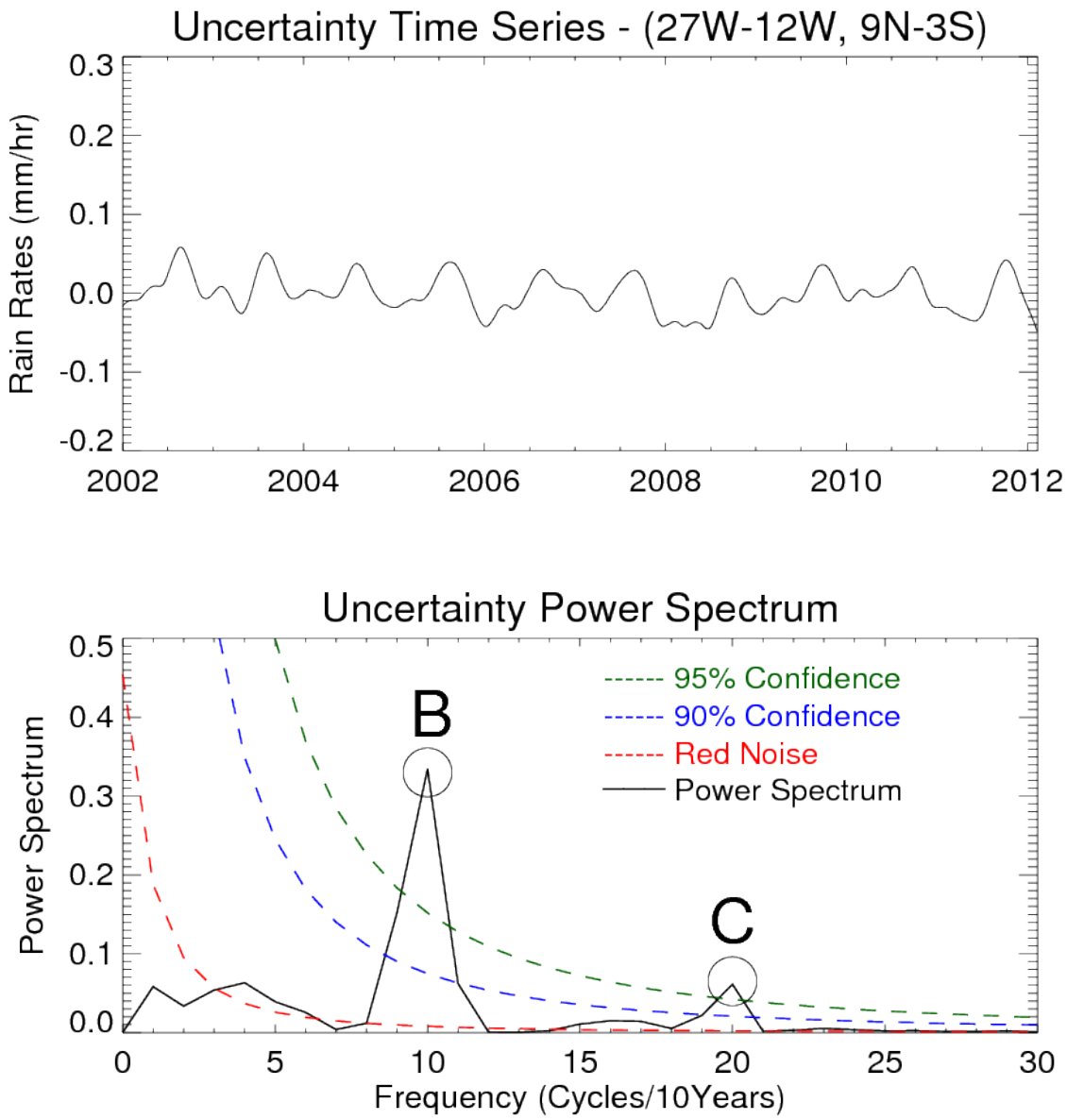

Figure 4.7 FFT Analysis over the Eastern Equatorial Pacific

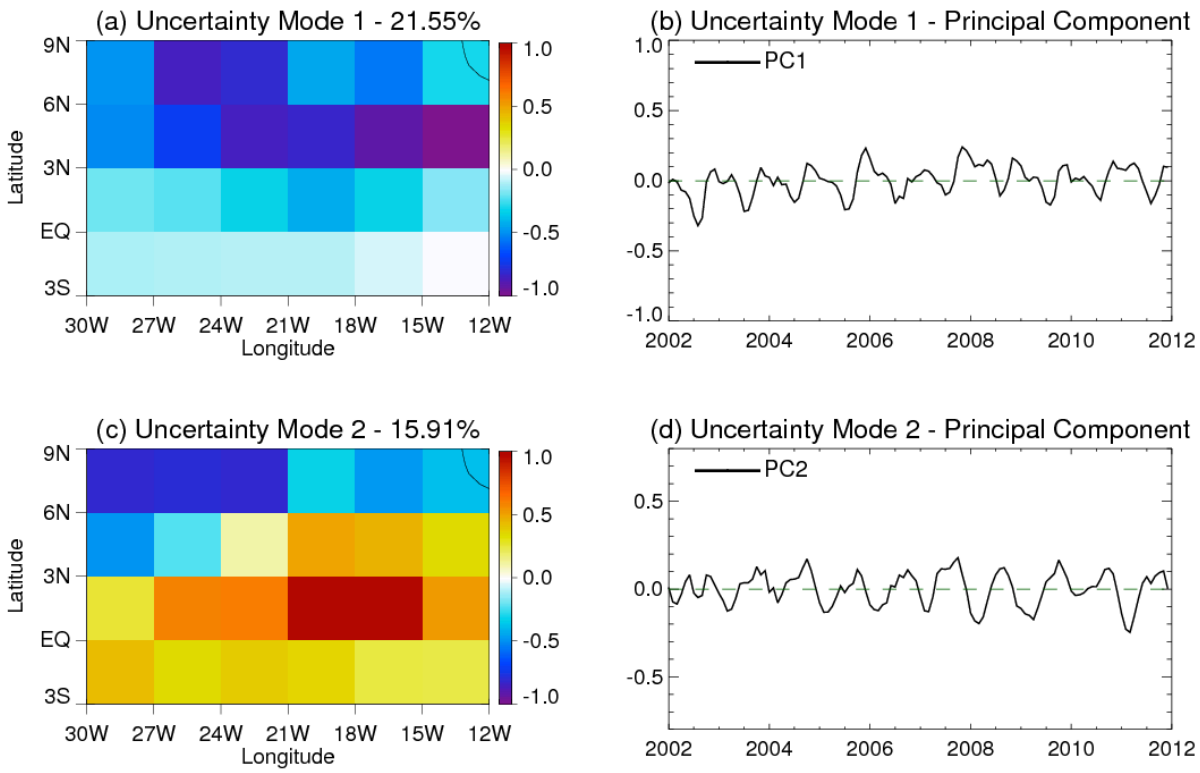

Figure 4.8 EOF Analysis over the Eastern Equatorial Atlantic

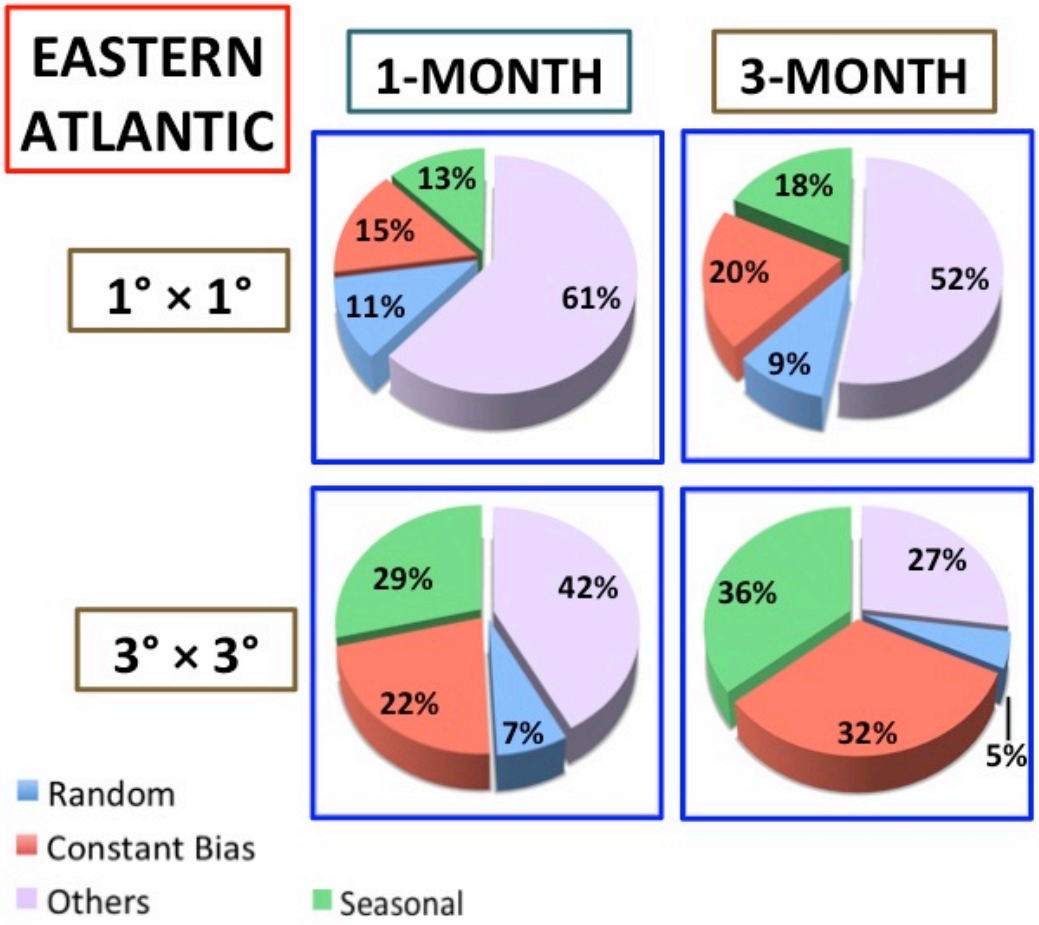

Figure 4.9 Major Uncertainty Sources Partitions over the Eastern Equatorial Atlantic under Various Spatial and Temporal Resolutions

TABLES

Table 3.1 TMI Performance Characteristics (Kummerow et al. 1998)

Channel	**Center Freq. (GHz)**	**Polari-zation**	**Bandwidth (MHz)**	**Sensitivity (K)**	**IFOV (km x km)**	**Sampling Interval (km x km)**	**Integr-ation Time (m/sec)**	**Main Beam Effic-iency (%)**	**Beam width (deg)**
1	10.65	V	100	0.63	63 x 37	13.9x9.1	6.6	93	3.68
2	10.65	H	100	0.54	63 x 37	13.9x9.1	6.6	93	3.75
3	19.35	V	500	0.50	30 x 18	13.9x9.1	6.6	96	1.90
4	19.35	H	500	0.47	30 x 18	13.9x9.1	6.6	96	1.88
5	21.3	V	200	0.71	23 x 18	13.9x9.1	6.6	98	1.70
6	37.0	V	2000	0.36	16 x 9	13.9x9.1	6.6	91	1.00
7	37.0	H	2000	0.31	16 x 9	13.9x9.1	6.6	92	1.00
8	85.5	V	3000	0.52	7 x 5	13.9x4.6	3.3	82	0.42
9	85.5	H	3000	0.93	7 x 5	13.9x4.6	3.3	85	0.43

Table 3.2 List of All MJO Events (Elsaesser and Kummerow 2012)

No. of Events	Starting Date	Ending Date	Days of Duration	Dates of Maximum Strength
1	20040213	20040406	56	20040228
2	20040627	20040819	51	20040711
3	20040806	20040914	42	20040829
4	20040912	20040925	16	20040916
5	20040916	20041020	37	20041006
6	20050205	20050309	35	20050221
7	20050531	20050708	41	20050625
8	20050703	20050814	45	20050730
9	20050811	20051007	56	20050827
10	20051020	20051114	28	20051104
11	20051106	20051116	13	20051111
12	20051120	20060208	83	20051129
13	20051129	20060220	76	20060122
14	20060212	20060302	21	20060224
15	20060309	20060412	37	20060324
16	20060417	20060426	12	20060422
17	20061007	20061030	22	20061016
18	20070115	20070129	17	20070122
19	20070206	20070417	67	20070228
20	20070312	20070325	14	20070317
21	20070427	20070505	11	20070501
22	20070704	20070822	52	20070720
23	20070819	20071007	49	20070915

REFERENCES

Adeyewa, Z. D., and K. Nakazawa, 2003: Validation of TRMM radar rainfall data over major climatic regions in Africa. *J. Appl. Meteor.*, **42**, 2, 331-347.

Adler, R. F., G. Gu, and G. J. Huffman, 2012:Estimating climatological bias errors for the Global Precipitation Climatology Project (GPCP). *J. Appl. Meteor. Climatol.*, **51**, 1, 84-99.

Allison, L. J. E. B. Rogers, T. T. Wilheit, and R. W. Fett, 1974: Tropical cyclone rainfall as measured by the Nimbus Electrically Scanning Microwave Radiometer. *Bull. Amer. Meteor. Soc.*, **55**, 9, 1074-1089.

Bauer, P. J. F. Mahfouf, W. S. Olson, F. S. Marzano, S. D. Michele, A. Tassa, and A. Mugnai, 2002: Error analysis of TMI rainfall estimates over ocean for variational data assimilation. *Quart. J. Roy. Meteor. Soc.*, **128**, 584, 2129-2144.

Berg. W., T. L'Ecuyer, and C. Kummerow, 2006: Rainfall climate regimes: the relationship of regional TRMM rainfall biases to the environment. *J. Appl. Meteor. And Climatol.*, **45**, 434-454.

Berg, W., T. L'Ecuyer, and S. C. van den Heever, 2008: Evidence for the impact of aerosols on the onset and microphysical properties of rainfall from a combination of active and passive satellite sensors. *J. Geophy. Res.*, **113**, D14S23, doi:10.1029/2007/JD009649.

DeMoss, J. D., and K. P. Bowman, 2007: Changes in TRMM rainfall due to the orbit boost estimated from buoy rain gauge data. *J. Atmos. and Ocean Tech.*, **24**, 9, 1598-1607.

Elleman, R. 1997: Predicting the Madden and Julian Oscillation Using a Statistical Model. (unpublished)

Elsaesser G., and C. D. Kummerow, 2012: Satellite-Derived Cold Pool Activity, Convection and Moisture Evolution During MJO Initiation in the Indian Ocean. *AGU Fall Meeting Abstracts*, **1**, 2012.

Ferraro, R. R., E. A. Smith, W. Berg, and G. J. Huffman, 1998: A screening methodology for passive microwave precipitation retrieval algorithms. *J. Atmos. Sci.*, **55**, 9, 1583-1600.

Giannini, A., J. C. Chiang, M. A. Cane, Y. Kushnir, and R. Seager, 2001: The ENSO teleconnection to the tropical Atlantic Ocean: contributions of the remote and local SSTs to rainfall variability in the tropical Americas. *J. Climate*, **14**, 24, 4530-4544.

Gloersen, P. and L. Hardis, 1978: Scanning multichannel microwave radiometer (SMMR) experiment. *In: Madris, C.R. (ed.) Nimbus 7 User's Guide*. NASA/GSFC, Greenbelt, MD, 213-245 pp.

Grody, N. C., 1991: Classification of snow cover and precipitation using the Special Sensor Microwave Imager. *J. Geophy. Res.: Atmospheres (1984-2012)*, **96**, D4, 7423-7435.

Hitschfeld, W., and J. Bordan, 1954: Errors inherent in the radar measurement of rainfall at attenuating wavelengths. *J. Meteor.*, **11**, 58-67.

Hou, A. Y., and Coauthors, 2014: The Global Precipitation Measurement Mission. *Bull. Amer. Meteor. Soc.*, **95**, 5, 701-722.

Iguchi, T., and R. Meneghini, 1994: Intercomparison of single-frequency methods for retrieving a vertical rain profile from airborne or spaceborne radar data. *J. Atmos. and Oceanic Tech.*, **11**, 6, 1507-1516.

Iguchi, T., T. Kozu, R. Meneghini, J. Awaka, and K. I. Okamoto, 2000: Rain-profiling algorithm for the TRMM precipitation radar. *J. Appl. Meteor.*, **39**, 12, 2038-2052.

Kawanishi, T., and Coauthors, 2003: The Advanced Microwave Scanning Radiometer for the Earth Bbserving System (AMSR-E), NASDA's contribution to the EOS for global energy and water cycle studies. *Geoscience and Remote Sensing, IEEE Transactions on*, **41**, 2, 184 – 194, doi:10.1109/TGRS.2002.808331.

Kummerow, C., W. S. Olson, and L. Giglio, 1996: A simplified scheme for obtaining precipitation and vertical hydrometeor profiles from passive microwave sensors. *IEEE Trans on Geosci. and Remote Sensing*, **34**, 1213-1232.

Kummerow, C., W. Barnes, T. Kozu, J. Shiue, and J. Simpson, 1998: The tropical rainfall measuring mission (TRMM) sensor package. *J. Atmos. and Ocean Tech.*, **15**, 808-816.

Kummerow, C., and Coauthors, 2001: The evolution of the Goddard Profiling Algorithm (GPROF) for rainfall estimation from passive microwave sensors. *J. Appl. Meteor.*, **40**, 1801-1820.

Kummerow, C. D., R. Ringerud, J. Crook, D. Randel, and W. Berg, 2011: An observationally generated a-priori database for microwave rainfall retrievals. *J. Atmos. And Oceanic Tech.*, **28**, 113-130, doi: 10.1175/2010JTECHA1468.1.1.

Liu, C., and E. Zipser, 2005: Global distribution of convection penetrating the tropical tropopause. *J. Geophy. Res.: Atmospheres (1984-2012)*, **110**, D23.

Maggioni, V., M. R. Sapiano, R. F. Adler, Y. Tian, and G. J. Huffman, 2014: An Error Model for Uncertainty Quantification in High-Time-Resolution Precipitation Products. *J. Hydrometeor.*, **15**, 3, 1274-1292.

Masunaga, H., T. Iguchi, R. Oki, and M. Kachi, 2002: Comparison of rainfall products derived from TRMM microwave imager and precipitation radar. *J. Appl. Meteor.*, **41**, 8, 849-862.

McCollum, J. R., and R. R. Ferraro, 2003: Next generation of NOAA/NESDIS TMI, SSM/I, and AMSR-E microwave land rainfall algorithm. *J. Geophy. Res.: Atmospheres (1984-2012)*, **108**, D8.

Meneghini, R., T. Iguchi, T. Kozu, L. Liao, K. I. Okamoto, J. A. Jones, and J. Kwiakowski, 2000: Use of the surface reference technique for path attenuation estimates from the TRMM precipitation radar. *J Appl. Meteor.*, **39**, 12, 2053-2070.

Munchak, J., 2010: A Method to Combine Spaceborne Radar and Radiometric Observations of Precipitation. Ph. D. dissertation, Dept. of Atmospheric Science. Colorado State University, 132pp.

Munchak, S. J., C. D. Kummerow, and G. Elsaesser, 2012: Relationships between the raindrop size distribution and properties of the environment and clouds inferred from TRMM. *J. Climate*, **25**, 8, 2963-2978.

Nesbitt, S. W., and E. J. Zipser, 2003: The Diurnal Cycle of Rainfall and Convective Intensity according to Three Years of TRMM Measurements. *J. Climate*, **16**, 1456-1475.

Nesbitt, S. W., E. J. Zipser, and C. D. Kummerow, 2004: An Examination of Version-5 Rainfall Estimates from the TRMM Microwave Imager, Precipitation Radar, and Rain Gauges on Global, Regional, and Storm Scales. *J. Appl. Meteor.*, **43**, 1016-1036.

Oki, T., and S. Kanae, 2006: Global hydrological cycles and world water resources. *Science*, ***313***, 5790, 1068-1072.

Petkovic, V. and C. D. Kummerow. Personal communication.

Rajendran, K., and T. Nakazawa: Systematic differences between TRMM 3G68 PR and TMI rainfall estimates and the possible association with life cycle of convection. *SOLA*, **1**, 165-168.

Rodgers, C. D., 2000: *Inverse Methods for Atmospheric Sounding: Theory and Practice*. World Scientific Publishing, 240pp.

Smith, R. A., and C. D. Kummerow, 2013: A comparison of in situ, reanalysis, and satellite water budgets over the Upper Colorado River basin. *J. Hydrometor.*, **14**, 3, 888-905.

Spencer, R. W., 1986: A satellite passive 37-GHz scattering-based method for measuring oceanic rain rates. *J. Climate and Appl. Meteor.*, **25**, 6, 765-766.

Stephens, G. L., and C. D. Kummerow, 2007: The remote sensing of clouds and precipitation from space: A review. *J. Atmos. Sci.*, **64**, 3742-3765.

Strangeways, I., 2010: A history of rain gauges. *Weather*, **65**, 5, 133-138.

Taylor, J. R., 1997: *An Introduction to Error Analysis: The Study of Uncertainties in Physical Measurements*. University Science Books, 327pp.

Towneley, R., 1694: Observations on the quantity of rain falling monthly for several years successively. A Letter from Richard Towneley. *Trans. Roy. Soc.*, London, **18**, 52.

Wang, J., and D. B. Wolff, 2012. Evaluation of TRMM rain estimates using ground measurements over central Florida. *J. Appl. Meteor. Climatol.*, **51**, 5, 926-940.

Wang, N. Y., C. Liu, R. Ferraro, D. Wolff, E. Zipser, and C. Kummerow, 2009: TRMM 2A12 land precipitation product – Status and future plans. *J. Meteor. Soc. Japan A*, **87**, 237-253.

Wang, P. K., and D. E. Zhang, 1988: An introduction to some historical governmental weather records of China. Bull. *Amer. Meteor. Soc.*, **69**, 753-758.

Wild. M., D. Folini, C. Schär, N. Loeb, E. G., Dutton, and G. König-Langlo, 2013: The global energy balance from a surface perspective. *Climate Dynamics*, **40**, 11-12, 3107-3134.

Yamamoto, M. K., F. A., Furuzawa, A. Higuchi, and K., Nakamura, 2008: Comparison of diurnal variations in precipitation systems observed by TRMM PR, TMI and VIRS. *J. Climate*, **21**, 16, 4011-4028.